REPORT DOCUMENTATION PAGE

AFRL-SR-BL-TR-99-

$\partial 180$

1. AGENCY USE ONLY (Leave Blank)	2. REPORT DATE 99 July 08	3. REPORT TYPE AND DATES COVERED FINAL 98 July 15 through 99 July 14

4. TITLE AND SUBTITLE	5. FUNDING NUMBERS
Micro Laser Plasma Thrusters for Small Satellites	F49620-98-C-0038

6. AUTHOR(S)

Claude R. Phipps, Ph.D.

7. PERFORMING ORGANIZATION NAME (S) AND ADDRESS(ES) Photonic Associates 200A Ojo de la Vaca Road Santa Fe, NM 87505	8. PERFORMING ORGANIZATION REPORT NUMBER PHO0005
9. SPONSORING/MONITORING AGENCY NAME(S) AND ADDRESS(ES) Department of the Air Force Air Force Office of Scientific Research 801 North Randolph St. Room 732 Arlington, VA 22203-1977	10. SPONSORING/MONITORING AGENCY REPORT NUMBER 0002AA

11. SUPPLEMENTARY NOTES

12a. DISTRIBUTION/AVAILABILITY STATEMENT Approved for public release; distribution unlimited.	12b. DISTRIBUTION CODE

13. ABSTRACT (Maximum 200 words) Report developed under STTR contract for topic AF98T003

Micro- and nano-satellites will be from 100kg to as little as 1kg. However, microthrusters which produce the very small minimum impulse bits (MIB) needed to accurately point these satellites did not exist before we developed our micro laser plasma thruster (μLPT). The μLPT is an efficient, long life, low-thrust pulsed rocket engine which uses a high brightness semiconductor or glass fiber laser as a source of energy. It uses a simple low voltage semiconductor switch to drive the laser without using any electrical power in the off state. A lens brings the laser light output to a target within a very small spot, producing a spark or miniature jet, which provides the impulse. Advantages of the LPT relative to other engines are:

1. Specific impulse up to 2,000 seconds, much larger than competing techniques because of the high temperature produced by the focused laser
2. The smallest minimum impulse bit (MIB) of any thruster: 1 nano newton-second
3. A very large operating range for impulse generated by a single device (100,000 bits:1)
4. A nearly infinite force range in a single device

Potential total mass of a few ounces arising from the smallness and simplicity of the operating parts of the engine.

14. SUBJECT TERMS STST Report plasma, microsatelite, nanosatellite, picosatellite, propulsion, laser ablation, thruster		15. NUMBER OF PAGES 54
		16. PRICE CODE

17. SECURITY CLASSIFICATION OF REPORT UNCLASSIFIED	18. SECURITY CLASSIFICATION OF THIS PAGE UNCLASSIFIED	19. SECURITY CLASSIFICATION OF ABSTRACT UNCLASSIFIED	20. LIMITATION OF ABSTRACT

REF D

Standard Form 298 (Rev. 2-89)
Prescribed by ANSI Std. Z39-18
298-102

1. Overview of the LPT Program

1.1 Executive Summary

Commercial, scientific and military communities who field Low Earth Orbit (LEO) Satellites are now moving toward the concept of micro- and nano-satellite constellations, in which advancing technology permits linking networks of numerous, very small satellites to take the place of expensive, very large satellites. In many cases, due to their distributed nature, these constellations can accomplish tasks that could not be performed by single large spacecraft. Micro- and nano-spacecraft will be from 100kg to as little as 1kg mass.

However, microthrusters with very small minimum impulse bits (MIB) needed to accurately point these satellites did not exist before we developed our laser plasma thruster (LPT) in Phase I.

The μLPT is a low mass, efficient, long life, micro-thruster for microsatellites which uses a high brightness semiconductor or glass fiber laser as a source of energy. It uses a simple low voltage semiconductor switch to drive the laser without using any electrical power in the off state. A lens brings the laser light output to a target within a very small spot, producing a spark or miniature jet, which provides the thrust. Figure 1 shows how the device works.

Advantages of the LPT relative to other engines are:

1. Specific impulse (related to exhaust velocity) larger than competing techniques because of the high temperature produced by the focused laser

2. The smallest minimum impulse bit (MIB) of any thruster: 1 nano newton-second

3. A very large operating range for impulse generated by a single device (100,000 bits:1)

4. A nearly infinite force range in a single device

5. Potential total mass of a few ounces (to be demonstrated in Phase II), arising from the smallness and simplicity of the operating parts of the engine

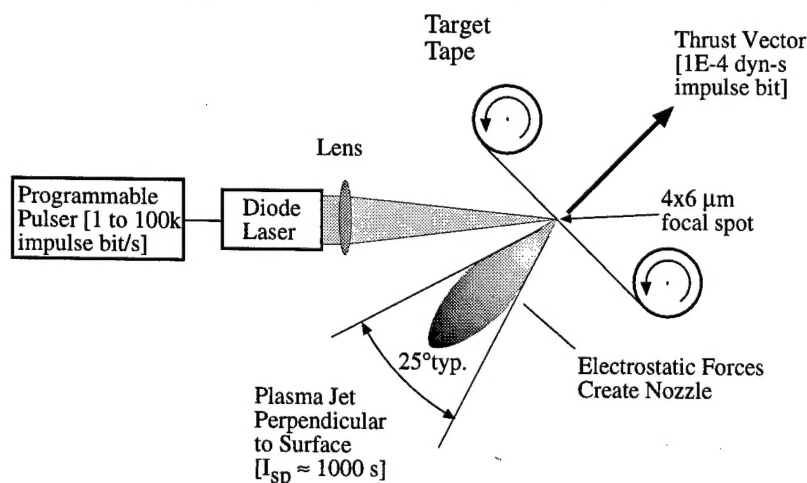6. Potential applicability to orbit raising in a higher power version.

Fig. 1. Illustrating the Laser Plasma Thruster (LPT)

The MIB discussed in the USAF requirement for this task (to which our Phase I project responded) is 1 nano newton-second [1E-4 dyn-s]. This is an impulse ten times smaller than the momentum of a flying mosquito. Applied at 500Hz, such an impulse would just levitate a 1mm diameter dot of typing paper.

Yet, such an MIB requirement is realistic. For a 10-kg, 20-cm-radius satellite at 500km altitude, ±1bit applied as torque controls drift of the center of its field of regard on the ground to ±5m/s. Applied in translation for stationkeeping, 1 bit gives a velocity change which, after a year, changes the position of the 10-kg satellite by 3km.

Our 1-watt LPT now generates 0.1 mN force; a 10-watt version of the Phase II engine will generate 1 mN, which is sufficient to raise a 10-kg LEO satellite 500 km in 30 days.

19990726 106

Scaledowns of conventional thruster designs to very small physical scale have been proposed to generate micro-impulses. Examples are miniature chemical rockets, pulsed gas thrusters, ion drives, plasma jets and "resistojets", which use the same principle as do inkjet printer heads.

However, behavior of these engines at small scales is not predicted by behavior at large scales. See § 1.3 below for a complete discussion of these effects.

We proposed, and have now proved in Phase I, this new technology for satellite orientation and propulsion, in which thrust is generated by the ablation jet produced by a focused, pulsed semiconductor laser. Thrust is always normal to the target surface. No nozzle is required to form the jet. Published data [see e.g. Phipps and Dreyfus 1993] shows that plasma electrostatic forces constrain the jet into a well-directed lobe. No new physics is required to understand very small scale operation at the 5μm-diameter focus. The laser energy required to produce a given impulse is well understood, based on our previous reported work. Electrical efficiency and specific impulse I_{sp} are similar to that of pulsed plasma thrusters (PPT's), but the LPT is much simpler and potentially much smaller, like a TV remote control. Its electrical pulser needs only produce logic-level voltages rather than kV. It uses no power when it is not "on". It can make a 100μs thrust pulse, anywhere from once a month to thousands of times a second, or it can simply be "on" all the time. Another plus is long life - the laser can easily outlast the satellite, and the precious "fuel" for the tiny rocket is used efficiently by heating it to high temperature during each spark.

We measured I_{sp} as large as 1,800 seconds in the engine's output midrange. Even at 1 MIB output, we measured I_{sp} up to 350 s. Limited by the 1 watt peak deliverable power of the Phase I diode, $I_{sp} = 300s$ can be considered typical. In other work, the author has measured specific impulse $I_{sp} = 7,000s$ using more powerful short-pulse lasers [Phipps and Michaelis 1994].

We measured momentum coupling coefficients (ratio of momentum produced to incident laser energy) C_m up to 25 dyn-s/J. This is among the largest values ever reported in the ablation literature for simple homogeneous materials. $C_m=10$ dyn-s/J was typical for our targets.

The ratio between the largest impulse we observed with our engine and the smallest in a single shot is 4.6 decades, from 16 kbits to 0.4 bits, as we varied laser pulsewidth from 100 μs to 300 ms.

Lacking the target transport mechanism to be developed in Phase II, we did not make measurements of force in continuous operation. However we did observe the engine working at 1kHz. Implicitly, we achieved 5.1 decades in force dynamic range during 1 second with a single LPT – 16 kbits/pulse at 3.3 Hz with 300ms pulsewidth (cw operation) vs. 0.4 bits/pulse at 1Hz. It is obvious that the LPT's force dynamic range can be nearly infinite depending on how infrequently the small impulse is applied. The maximum continuous force output from our 1-watt engine as configured for Phase I is 10 dyn or 0.1 milli-newton.

The plume produced by the LPT is a directed jet of atomic vapor or plasma rather than a cloud of chemical compounds
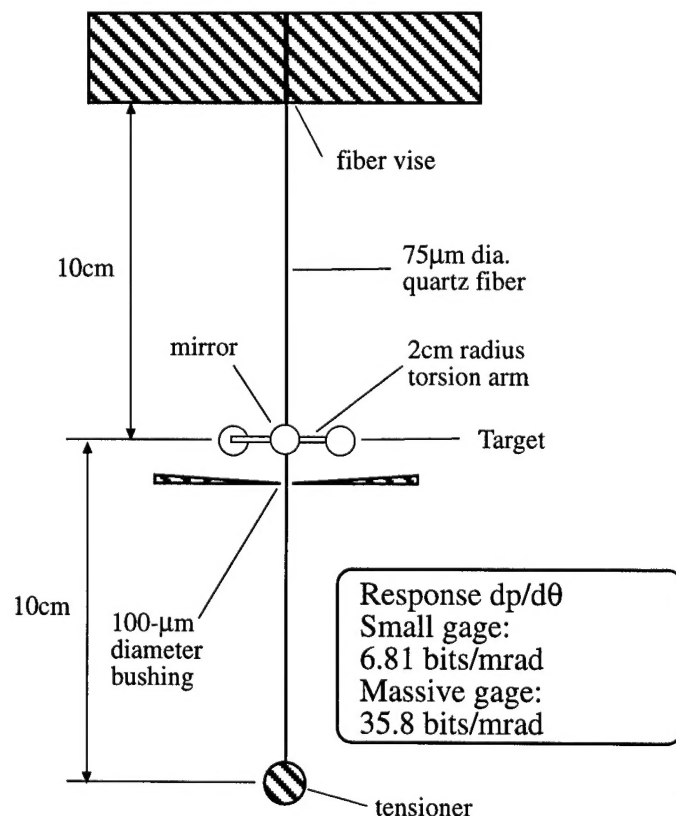

Figure 2: The torsion microbalance

which can condense on spacecraft optics, due to the high temperatures of the laser-surface interaction. We have observed no clouding of the target illumination optics during thousands of shots.

The most difficult part of this project was not making the thruster, but measuring impulses as small as 1 nano newton-sec. In order to measure the tiny impulses made by our microthruster, we built a torsion microbalance [Figure 2], using a glass fiber about the size of a human hair. The mirror shown deflects a monitor laser beam to a video station up to 3.4 meters distant for the most sensitive measurements. In this configuration, we sometimes have to wait during measurements while traffic finishes passing on the road 100 yards from the laboratory. Footsteps on the concrete floor next to the apparatus disturb it. A microscope inside the vacuum test chamber is used to position the target and determines the focused spot size on target.

1.2 How Laser Ablation Thrusters Work

Laser ablation [Dreyfus et al 1993] is the process by which a laser heats a solid surface sufficiently to eject atoms from the surface and is an important tool in microelectronics. This process is more complex than boiling a block of ice with a welding torch, in that "phase explosion" produces a jet of very hot vapor. The most momentum per joule of laser light is produced at or just beyond the threshold intensity for plasma formation. The nearly diffraction-limited beams of these new flare-type laser diodes can be focused to 5μm diameter at full-width half maximum (FWHM) with readily available lenses, so that 1 watt of laser power produces 1 MW/cm^2 on the target.

Table 1: Comparison of Micro-Thruster Types
[VL = Very Low, L = low, M = moderate, H = High, VH = Very high, EH = Extremely high]

Micro Thruster Type	Efficient Working Range	Operating Cost/Bit	"Fuel" Cost	Energy Efficiency	Relia-bility	Life in Use	I_{sp}
Laser	H	L: 1 device covers 5 decades	VL	H	VH	VH	1,000
Chemical	L	L - if batch fabricated	M	L	L - if High I_{sp}	1 shot	200
PPT	M	L - if batch fabricated	M	H	M	M	3,000
Gas Jets	----	L - if batch fabricated	H	L	H	L	100
Resisto-jets	---	L - if batch fabricated	M	L	M	M	50
Ion engines	M	H	L	H	L	M	5,000

1.3 Enabling Developments & Technologies

Laser ablation thrust has been proposed and seriously considered for a number of space applications during the past decade [Phipps and Michaelis 1993, Phipps 1992]. Several specific events in the past year have made on-board laser microthrusters the most compelling of these:

a) The availability of flare-type AlGaAs-based, single transverse mode semiconductor diode lasers [Figure 3] with brightness

$$B = \frac{P}{\lambda^2} = 230 \frac{MW}{cm^2 sterrad} \qquad [1]$$

These currently have an output of about 2 watts of nearly diffraction-limited power [Lang, *et al.* 1998] in the near-IR (970-nm wavelength) region. We realized that this brightness was adequate for the first time to enable rocket-like laser ablation thrust on a small scale from the spark formed by tightly focusing this beam on a solid surface in vacuum. Previous diodes were more than 100 times less bright, requiring kilowatts instead of watts to make the spark. Kilowatt-size diode bars and their power supplies are definitely too heavy and power hungry for microsatellites.

b) The development of such lasers with 35% electrical efficiency.

c) The routine focusing of such lasers to input 80% of their energy into a 6-μm diameter aperture for fiber-optics work.

d) Demonstration of mean-time-between-failure (MTBF) of 1 million hours in such lasers

In contrast, there are obvious problems with scaling down the pulsed plasma thruster (PPT), microchemical thruster and other conventional engine types to microscale.

Fig. 3. The Flare-type, High Brightness Diode Laser
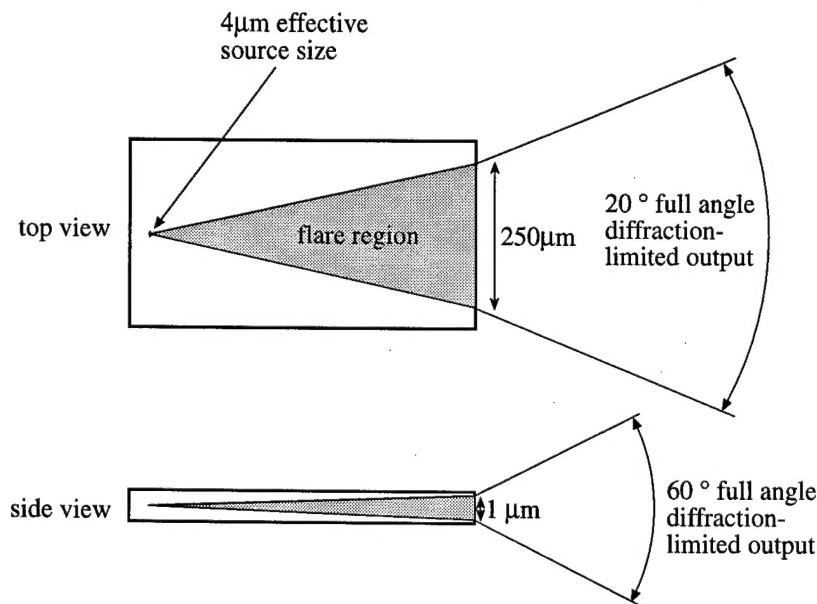
Some of these problems are:

a) New physical regimes are entered when the characteristic dimensions of the nozzles in such devices are so small that gas flow can no longer be characterized by the theory of viscous fluid flow. The assumption of a continuum on which fluid dynamics is based disappears when the mean free path is no longer much smaller than the nozzle diameter. For a 1μm nozzle, this assumption is strongly compromised at 10 bar pressure.

b) Further, boundary layer effects become dominant in μm-scale nozzles, an important complication for pulsed gas jets, micro chemical thrusters and micro PPT's.

c) In the case of micro PPT's, breakdown thresholds are not tabulated for such small electrode separation and not easily extrapolated from existing data. PPT's also have the problem of large high voltage power supplies.

d) There is no technology other than the LPT which has demonstrated such a small MIB.

In order to reach the intensities required to produce plasma on a surface with a 1-watt laser, it is necessary to create small focal spots, ranging from 5μm to 200μm depending on the laser pulsewidth being used. We had peak intensity up to $1MW/cm^2$ and fluence (energy density) up to 300 kJ/cm^2 available on target for our tests. Creating the smallest spot size, important for

producing small impulses, is not simple, but not as demanding as the technology routinely used to read the dots on a CD.

For midrange and large impulses, we found the spot size not to be very critical.

2. Technical Objectives

The objectives in our Phase I statement of work are:

a) Measure very small impulses at the level of 1E-4 dyn-s during 100μs with 10% accuracy, design and build impulse gage and calibrate it in the vacuum chamber.

b) Demonstrate a dynamic range of 100,000 from about 1 bit/s in a single LPT.

c) Match the impulse produced with theoretical predictions.

d) Determine the best algorithm for obtaining a large dynamic range.

e) Achieve and maintain 4x6 μm and larger foci with low jitter and compute target interaction parameters.

f) Measure parameters of the laser produced plasma, test laser operation and install optical diagnostics.

g) Measure and verify angular distribution of plume flux.

h) Select best target materials.

i) Assess feasibility of the LPT microthruster.

During Phase I, we completed all elements of our statement of work using facilities and personnel at UNM/New Mexico Engineering Research Institute.

3. Technical Accomplishments

3.1 Major achievements correlated to work statement objectives [in brackets]

- [a] We easily measured minimum impulse bits (MIB) equal to one billionth of a newton-second (1E-4 dyne-s) with 10% accuracy, and 1E-5 dyne-s with 50% accuracy [Annex I]. We demonstrated a dynamic range from 0.4 to 16,000 MIB's from a single LPT engine due to a single laser pulse.

- [b] Although the pulser provided with the laser by SDLI is not configured to make pulses longer than 300 ms, we showed that we could implicitly achieve 5 decades in dynamic range of force in one second with a single LPT just by comparing the above response of 16,000 bits per pulse at a 3.3Hz repetition rate to the minimum output of 0.4 bits/pulse at 1Hz giving a dynamic range of 120,000.

- [e] We repeatedly measured laser-ablation impulse produced by a single high-brightness laser diode with 1 watt peak power focused to a 5-μm (0.0002 inch) spot.

- We measured momentum coupling coefficients C_m up to 25 dyn-s/J. This is among the largest values ever reported in the ablation literature for simple homogeneous materials.

- We saw specific impulse of the laser-produced thruster jet up to 1800 seconds. Widely used competing technologies give 50 seconds (resistojets) and 200-300 seconds (chemical rockets).

- Sixteen materials were studied in 48 data runs producing over 400 impulse data points.

- The laser diode fired thousands of shots without any deterioration in performance.

- We built two torsion balances, one 5 times more sensitive than the other, to do the impulse measurements.
- We noticed no degradation of the target illumination optics due to target debris.
- Results obtained agree well with expectations and theory.

We believe that each of the above accomplishments are first-time achievements, not reported previously in the literature of laser interaction with surfaces.

3.2 Negative results

- [f, g] Using a sensitive plasma detector which we built that was capable of detecting $Q_{min} = 2.4nC$ (1.5E10 electron charges) and subtending 1 sterradian 1 cm from the target, we failed to detect any plasma signal. This result is consistent with an ionization fraction $\eta_i < 1.4E-6$ in plume. Analysis indicates we were just below plasma threshold with maximum target intensity of 310 kW/cm^2 delivered to a 5μm spot [see Annex V].

- We could not produce impulse on targets with low surface absorptivity and/or high thermal conductivity (e.g., aluminum, fiberglass, cellulose nitrate, kapton, pressed graphite, black anodized aluminum - see Annex II) using a 1-watt laser. [See Annex V for discussion]

3.3 Other completed work statement objectives

The remaining objectives not listed above are discussed in the following places in this report:

- **[c]** Annex IV

- **[d]** §3.4 of this report, immediately following.

- **[h]** Annex II

- **[i]** §3.6 of this report.

3.4 Target illumination algorithm [objective d]

[See the discussion surrounding Figures 11–15 in §3.7.2 following] We found that two target illumination spot sizes, $d_{s1} = 5.2$μm and $d_{s2} = 200$μm fullwidth at half-maximum (FWHM) were adequate for all purposes we explored. The available range was set on the low end by minimum possible with the experimental setup.

The small spot size d_{s1} was important for getting coupling at all with pulses shorter than about $\tau = 5$ ms [compare Figures 12 and 13 following]. The large spot size d_{s2} was useful, though not crucial, for getting the best coupling coefficient for pulses up to $\tau=300$ms, the longest duration possible with the SDLI laser pulser provided with the laser. Spots larger than d_{s2} were not useful because no further benefit was achieved, but coupling begins to degrade due to inadequate fluence above this value.

The reason for this is that, after the target is burned through, no more impulse is generated. For 200-μm diameter illumination spot size our typical 175-μm-thick targets were burned through after pulse duration exceeded 50ms, and burnthrough was not severe until $\tau=150$ms. On the other hand, for 5-μm spots, burnthrough started at 10ms, decreasing coupling efficiency above that pulse duration, consistent with the trend of C_m vs. pulsewidth in Figure 12 (blue triangles).

Since all successful targets had about the same thermal diffusivity, the algorithm we developed depends only on pulse duration τ as follows:

IF 100μs < τ< 50ms	THEN	d_{s1}
IF τ >= 50ms	THEN	d_{s2}

Because the radial spacial profile of the focused laser pulse is not a "square hat" but a radial exponential [see Figure 9], it is only important to achieve very small spot size when making impulses of a few bits with short (e.g., 100μs) pulses. This is made visually clear in Figure 11.

3.5 Impulse gage

Our impulse gage is easily capable of measuring one MIB [Figure 2 & Annex I]. It can even measure light pressure (far smaller than ablation pressure). Annex I describes the gage, the gage setup, its theory of operation and its calibration.

3.6. Feasibility of the LPT Microthruster [objective i]

Figure 4 shows our concept for a commercial LPT microthruster. We strongly believe this device has commercial potential. We have demonstrated the advantages that we set out to demonstrate, which are summarized in §1.1. There are no deficits of which we are aware.

One thousand seconds is NOT a fundamental limit for this technology, but is due to the limitations of 1W peak laser power and 5μm minimum spot size. Specific impulse is determined by ablation temperature, which depends on the laser intensity (W/cm^2) we are able to deliver to the target. Values as large as 7000 seconds have been measured by the PI in other laser produced plasmas [Phipps *et al.* 1994].

Figure 4 is an outline drawing of a possible commercial thruster. In the Figure, the target transfer mechanism is visualized as counter-rotating disks to eliminate net torque to the spacecraft. Note
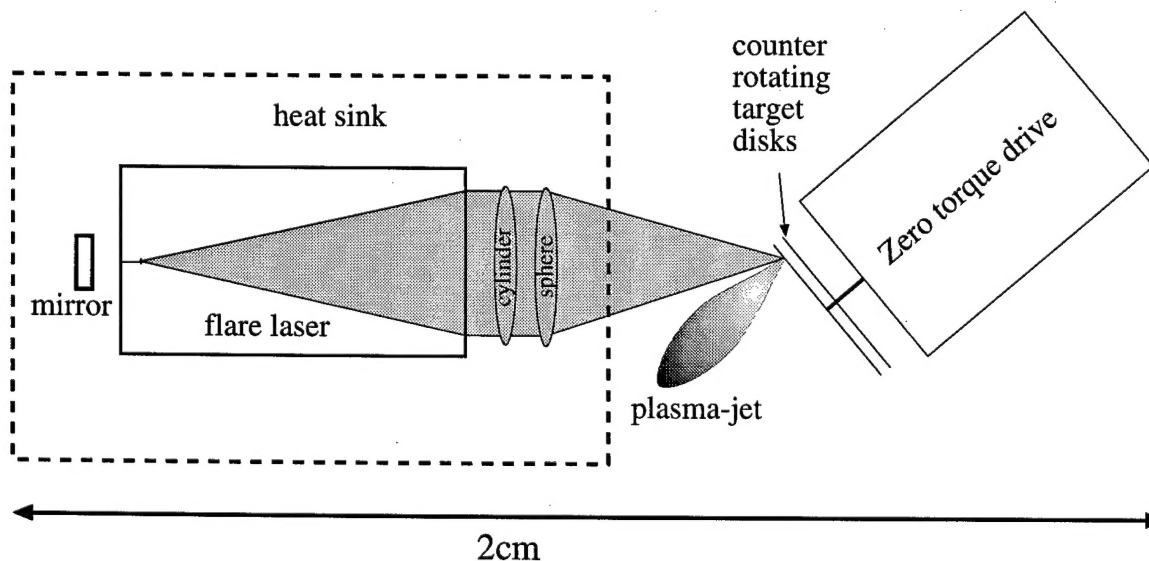
Figure 4: Conceptual Advanced Application Thruster

that linear velocity need not be greater than <u>0.2 mm/s</u> for continuous operation. Technology for focus and alignment need not be as precise as that customarily used in cheap, modern entertainment CD drives.

Developments required on the way to a prototype engine include (but are not limited to):

a) A target transport mechanism to advance the target material across the laser focus and permit continuous repetitive operation for the life of the on-board ablator

b) A passive thermal pathway design appropriate for dissipating laser-generated heat to space.

3.6.1 Commercial Potential of the µLPT

Case A: µLPT for microsatellite orientation

Basis: Sales price: $50k per unit in quantities of 10 - 20

Time Period	Market Potential (units)	Dollar volume
2000 – 2001	6 spacecraft x 6 thrusters = 36	$2 million
2002 – 2005	10 spacecraft x 6 thrusters = 60	$3 million
2006 – 2010	100 spacecraft x 6 thrusters = 600	$30 million

Case B: LPT for microsatellite orbit raising and stationkeeping

Basis: Sales price: $250k per unit in quantities of 10 - 20

Time Period	Market Potential (units)	Dollar volume
2000 – 2001	6 spacecraft x 1 thruster = 6	$1.5 million
2002 – 2005	10 spacecraft x 1 thruster = 10	$2.5 million
2006 – 2010	100 spacecraft x 1 thruster = 100	$25 million

We estimate total market at $64M for just these applications over 10 years. Leverage for funding this project is greater than 100:1.

3.6.2 Potential Customers

Teledesic Corp., Hughes, Motorola (for enhancement of the Iridium satellite system), Caltech Jet Propulsion Laboratory, NASA/Godard Spaceflight Center, US Air Force Research Laboratory Space Vehicles Directorate (Kirtland AFB).

3.6.3 Commercialization Plan

Photonic Associates is highly interested in commercializing LPT's for micro- and nanosatellites. This is a novel invention, and a key stepping-stone to development of LPT's for a broad range of applications. To accomplish commercialization of µLPT's, PA will undertake the following steps:

- Develop a useful, tested prototype LPT during our proposed Phase II STTR project.

- File patent applications for proprietary aspects of our invention. This step is <u>currently in process</u>, at the stage of prior art search, in partnership with the University of New Mexico.

- Team with a partner who has strong manufacturing capabilities and good access to capital.

- Develop a business plan. The plan may include investment in high brightness glass fiber development, to reduce cost, increase performance, and tailor performance to requirements.

- Obtain early phase venture capital to back this plan.

- Develop an initial line of miniature thruster products which meet the market in §6.1.

- Market the products to entities identified in §6.2

- Make further plans for LPT's based on experience with the marketing effort.

- Develop an expanded business plan for building and marketing macro LPT's and related systems, based on lessons learned in earlier phases.

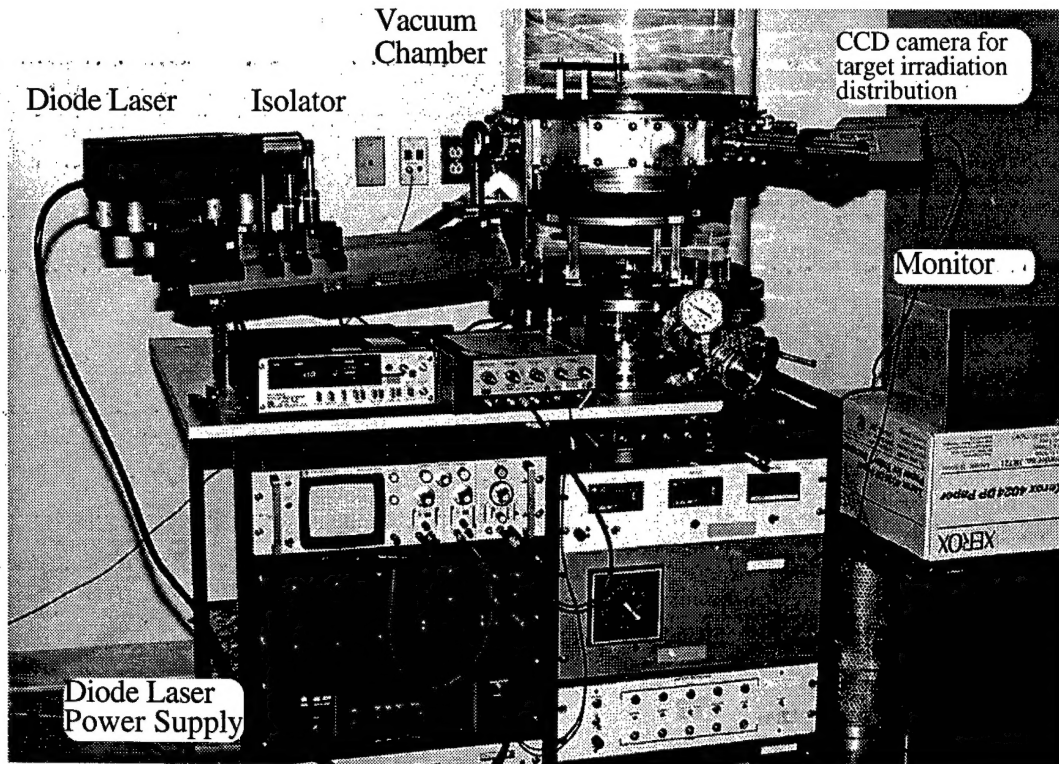- Go for second phase venture capital.

3.7 Experimental Setup
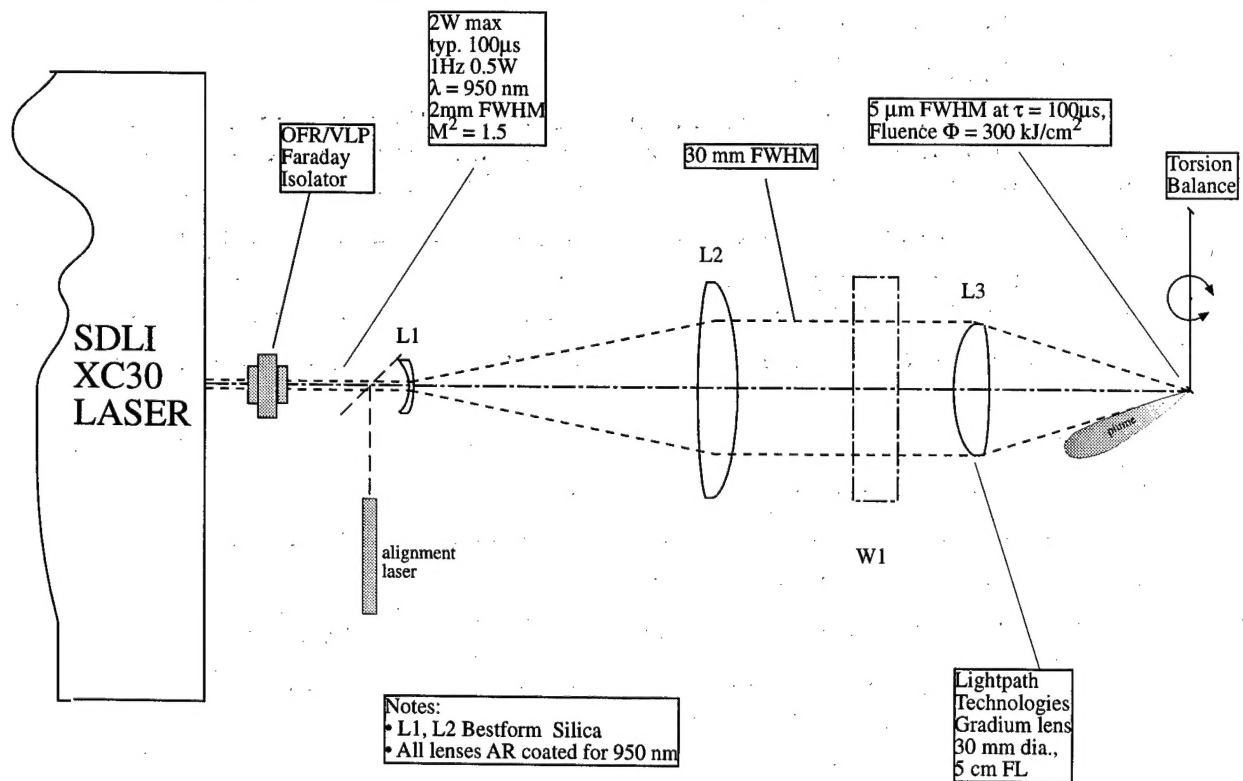

Figure 5: Target irradiation setup

Figure 6: Optical schematic drawing (top view)

Figure 5 shows the target test setup. The Spectra-Diode Labs XC-30 flare-type high-brightness laser is external to the chamber. The test beam is introduced to the chamber as indicated in Figure 6, via a 10X beam expansion telescope (L1-L2) and then focused to a 5-μm diameter spot by an axial gradient lens which behaves like an asphere.

Figure 7 shows the optical layout in and around the vacuum chamber

3.8 Major results obtained

3.8.1 Focal Spot Size
[work stmt objective e]

Figure 8 shows a typical beam intensity trace, and Figure 9 shows the statistical average of several measurements. We could repeatedly
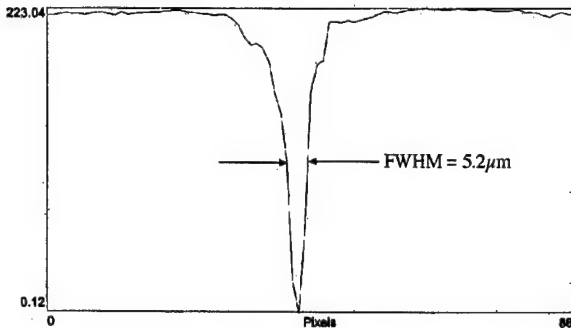
Figure 8: Beam diameter on target
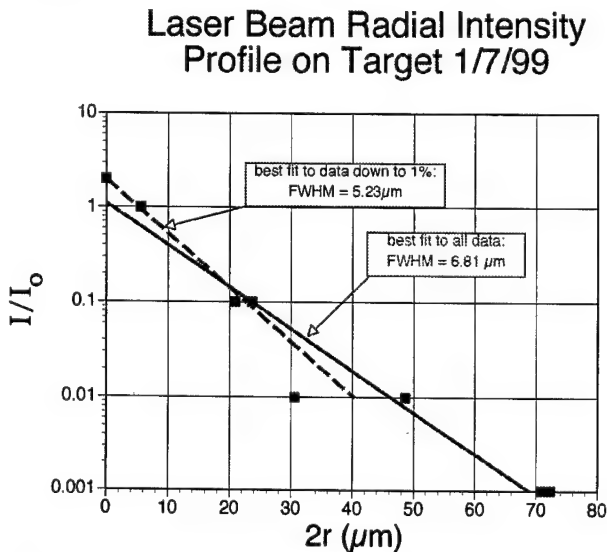
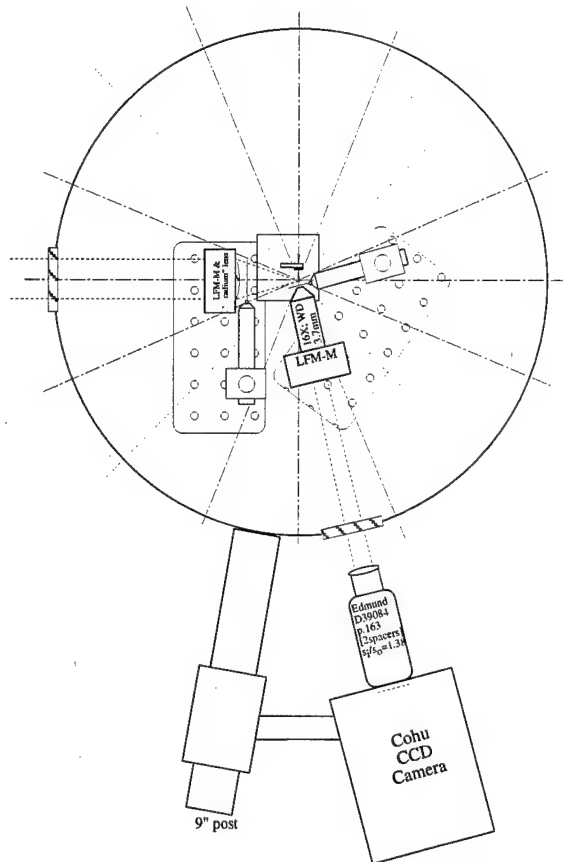**Figure 9: Data down to 1% of peak is consistent with 5.2 μm diameter**

Figure 7: In-chamber optical arrangement (top view)

obtain focal spot diameters of 5.2μm, which meets the requirements of our work statement. Jitter was less than 25%, which was the minimum measurable diameter in a single measurement, since such a spot size illuminated only 4 pixels on our CCD camera using the highest magnification microscope objective that would not interfere with the ablation laser beam.

The position of external lens L3 is a coarse adjustment that translates to a very fine adjustment of the axial position of the beam focus relative to the target, with a leverage of 60:1 [see figure 10]. Using this feature, we could carefully adjust the focal spot size after the test chamber was pumped down. This capability was especially important with the 5.2μm spots, but could also produce defocused spots of size 100 and 200μm, which we used to see how coupling varied with fluence. These larger spot sizes on target were also important for obtaining the best possible coupling at long (>50ms) pulse durations (see Annex IV).
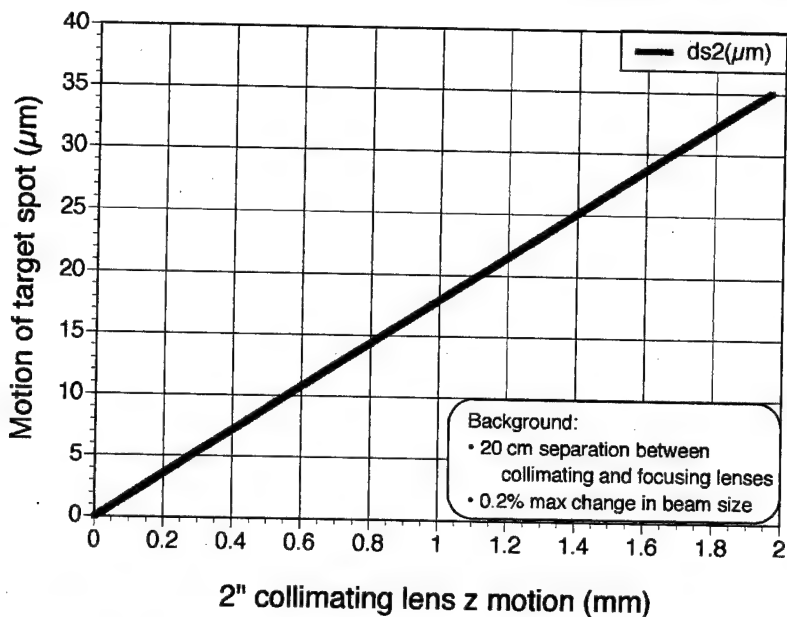
Figure 10. Method for precision control of focal spot position
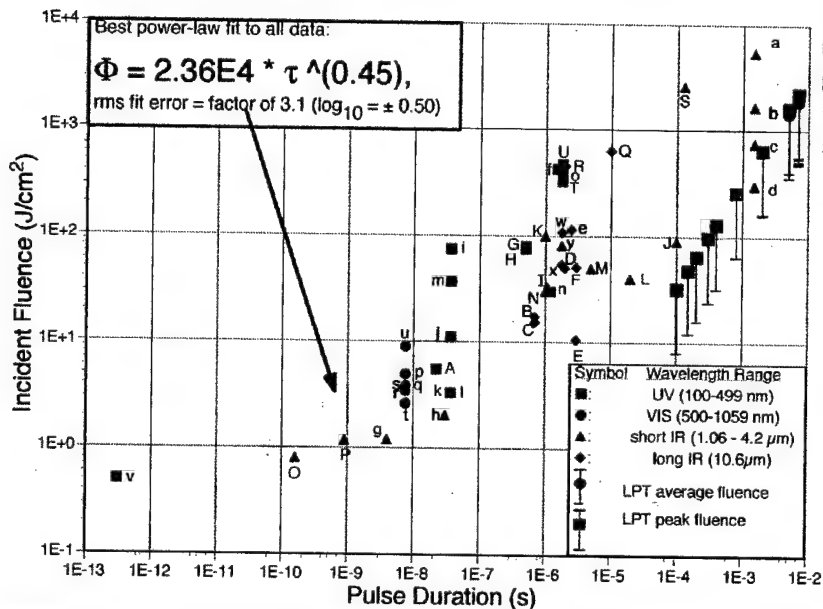
Figure 11: Optimum coupling fluence agrees well with predictions

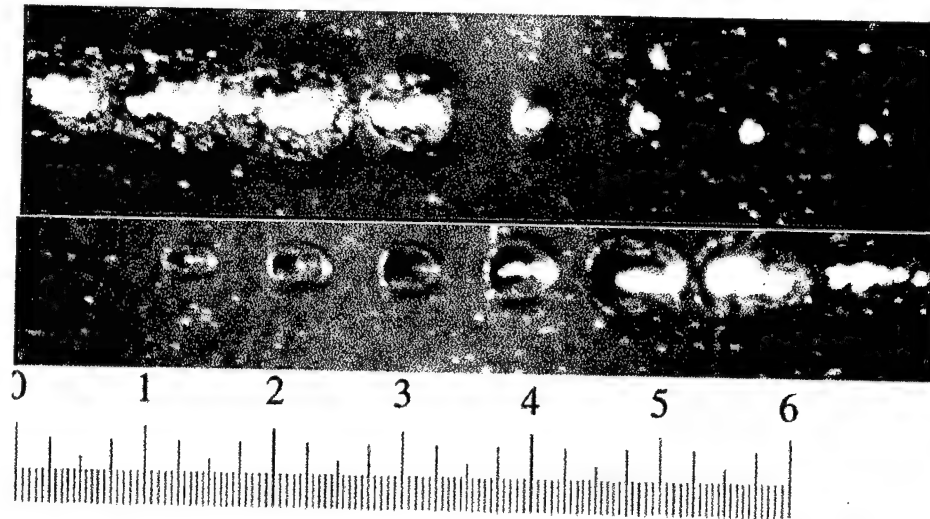### 3.8.2 Laser Ablation Impulse Measurements

Annex II is a summary listing of all targets tested, with data obtained. Annex III discusses the physics of laser momentum coupling during ablation of a solid surface - in particular how coupling data for 46 experiments reported in the ablation literature give a definite trend of peak coupling fluence vs. pulsewidth. In writing the Phase I proposal, we used this trend to predict how our LPT would operate.

Figure 11 shows how typical data we took during Phase I agrees with this prediction.

It was important to calculate, for each spot size and torsion pendulum mass, how much the target would move during the laser pulse which could be as long as 0.3 seconds. Annex IV shows how average fluence (shown in green in Figure 11) was calculated.

Figure 12 shows some typical target burn spots taken in vacuum, ranging in size from 20μm to 750μm in diameter. These were taken with (Upper) 5μm focal spot size and (Lower) 200μm spot size on PVC film.

Our best LPT performance results with various targets are shown in Figures 14-17.

Figures 14 and 15 compare the performance of black polyvinylchloride film at 5-μm laser spot size with what we obtained with 200-μm spotsize.

Note that I_{sp} is lower but C_m stays higher for longer pulses with the larger spotsize. Figure 12, taken with the target that produced the Figure 14 and 15 data, shows why. For 200-μm diameter

Figure 12: Photomicrographs of target burn spots ranging from 20μm to 750 μm in diameter, taken with 5μm (upper) and 200μm(lower) laser spot size. Graticule lines are spaced 50μm. Film was 175 μm thick.

illumination spot size, the 175-μm-thick film was burned through only after pulse duration exceeded 50ms and burn-through was not severe until $\tau=150$ms. On the other hand, for 5-μm spots, burn-through started at 10ms, decreasing coupling efficiency above that pulse duration, consistent with the trend of C_m vs. pulsewidth in

Table 2: Results for Best Targets [0.4W incident peak power]

Material	Max I_{sp} (s)	Max C_m (dyn-s/J)	Min Impulse (bits)	Max Impulse (bits)
Black PVC film	750	24	3	16,000
Black ink on thick paper	2,000	17	1	9,000
Black laser print on paper	150	10	2	5,000
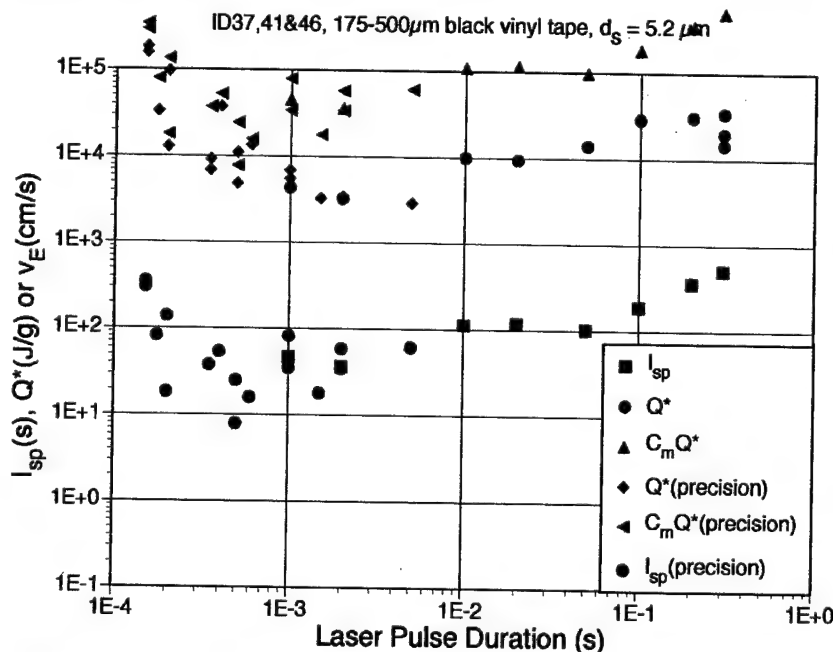
Figure 13: Q* values are determined by microscopic examination of the target

Figure 14 (blue triangles).

Figure 16 shows the performance of black printer's ink on 350-μm thick paper. Specific impulse was notable with this target, reaching values as large as I_{sp} = 2,000 s. Coupling remained high over much of the pulsewidth range. This data is interesting because of the tremendous range of impulse demonstrated from a single target.

If it is desired to have maximum coupling coefficient combined with very small MIB, Figure 17 shows the behavior of a target constructed from 10-μm mylar foil with a 1-2-μm black ink coating.
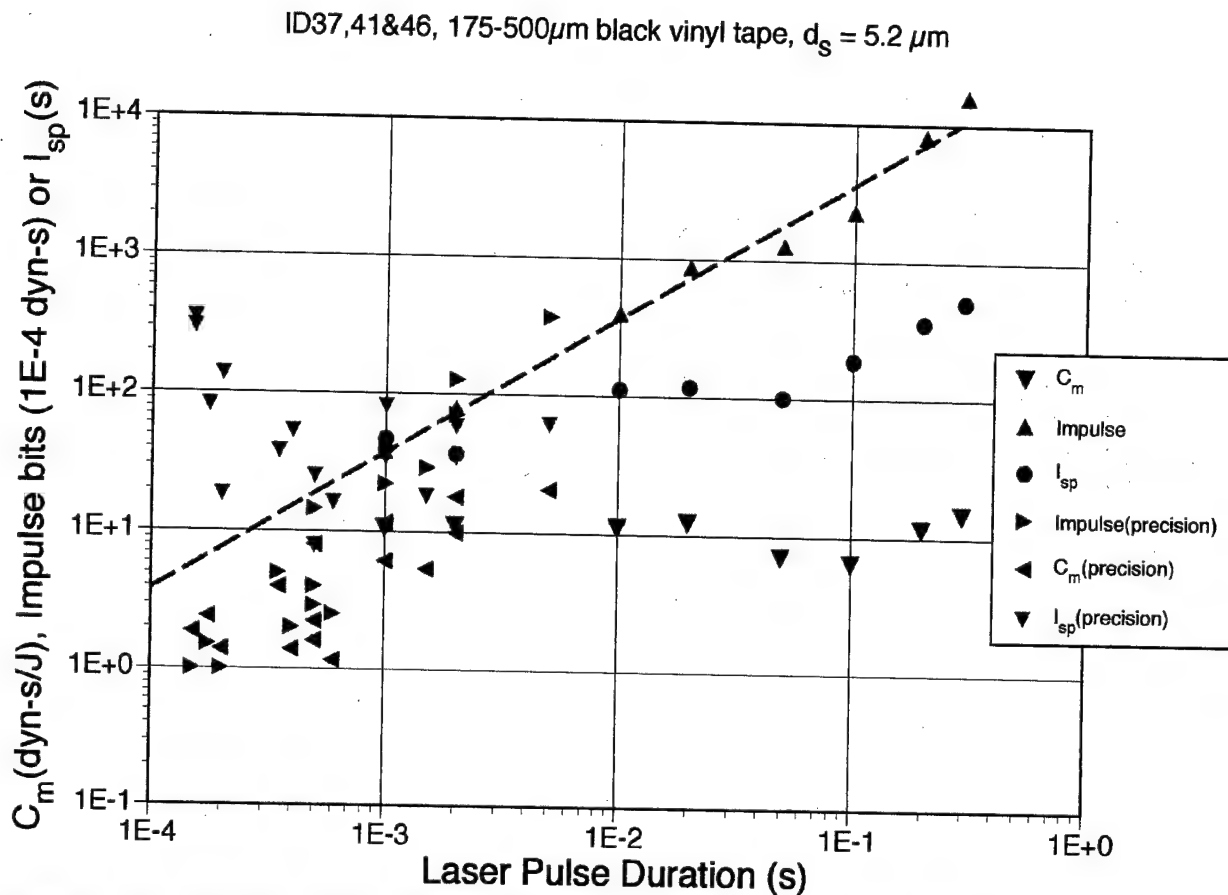
ID37,41&46, 175-500μm black vinyl tape, $d_S = 5.2\ \mu$m

Figure 14: Target: black PVC film 175μm thick. Laser spot size 5μm.

Figure 14 is our most thorough set of data for our best target material. It is composed of data from three sources: the heavy and light torsion balances, and the light balance with maximum range (340 cm) for the readout beam ("precision" data). Because this beam has to pass through a 2-inch target port window, "precision" data can be obtained only for a very limited range of deflections, so it is a special setup rarely used.

Note how C_m decreases, while Q* increases for the short pulses. This makes sense because of the increasing dominance of thermal conduction as an energy sink for very small ablation pits.

ID38, 330μm black vinyl tape, $d_S = 200\ \mu$m

Figure 15: Same as Figure 14, but $d_s = 200\mu$m.
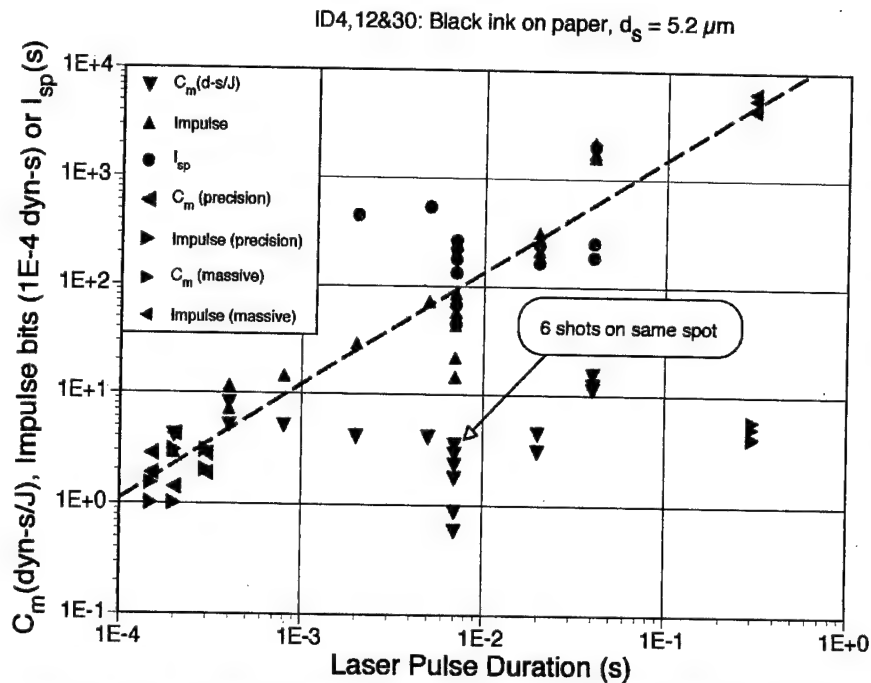
Figure 16: Black printer's ink on 350-μm-thick paper. Specific impulse reaches 2,000s. Coupling coefficient up to 17 dyne-s/J is seen.
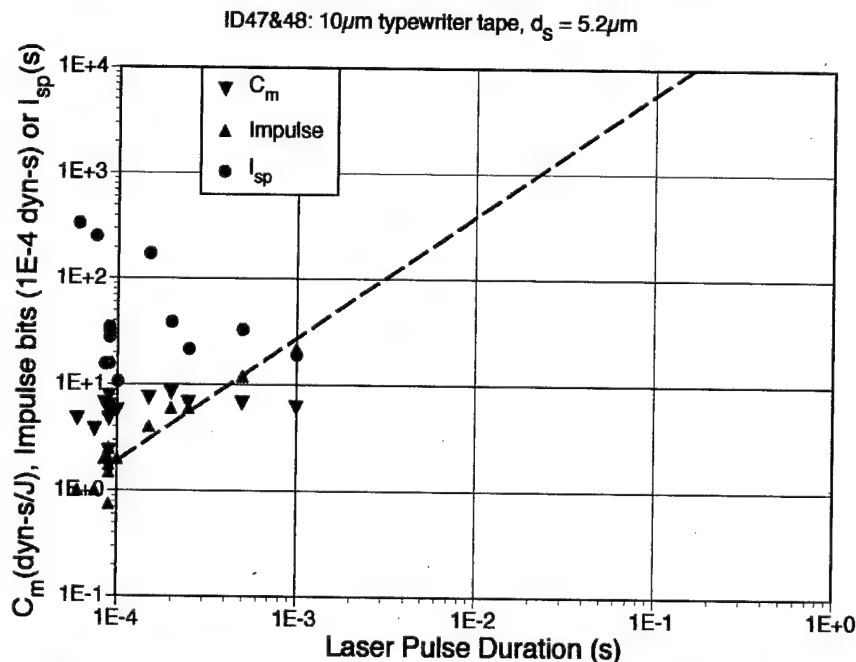
Figure 17: Black ink on 10-μm mylar foil. Excellent coupling coefficient together with acceptable I_{sp} are maintained down to 50μs pulsewidth and 0.75 bits.

3.8.3 Q* and Isp

Figure 13 shows the Q* data which is the basis for the I_{sp} values plotted in Figure 14. Annex III [Eqn. AIII.16] explains the connection between Q* and I_{sp}. Because the quantities of mass ablated are so small (often of order 10 nanograms), the only reasonable way to determine Q* is by careful microscopic measurement of the volume of each ablation pit. This was a bit tedious, but gave good results. We did this for each data point in the test series, and used the product $C_m Q^*$ to calculate I_{sp}.

3.8.4 "Gold Bar" Validation

Because we have so much coupling data, it is possible for the first time to assemble a 3-dimensional shape which shows how well experimental data support the dependence of peak coupling on fluence and pulsewidth predicted by Eqn. AIII.2 [Annex III].Figure 18 shows such a plot, assembled from the data for one particular target material. The height of the 3-dimensional shape in the figure is coupling coefficient C_m and the horizontal coordinates are fluence and pulsewidth. The gold bar plotted on the baseplane is the same one shown in Figure AIII.1 and Figure 11, showing that the agreement with the purely theoretical Eqn. AIII.2 prediction is quite good.

Target: Black ink on paper
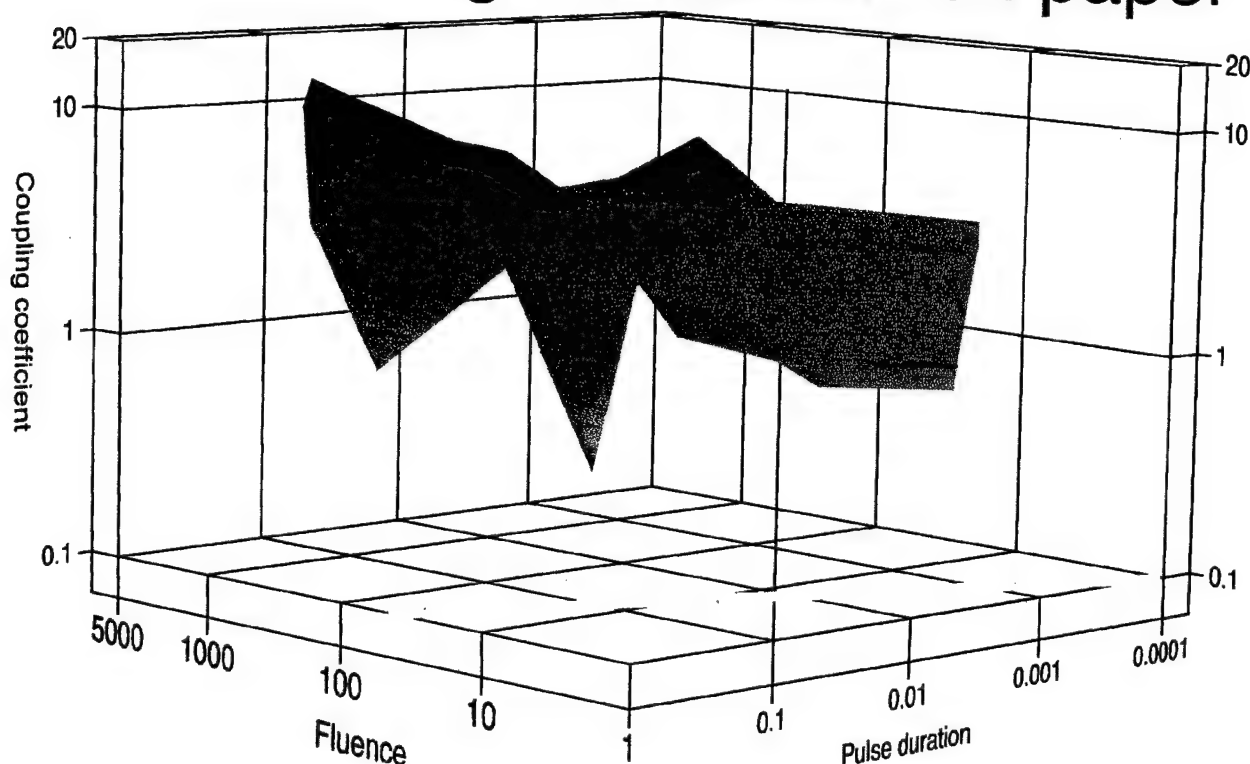
Figure 18: Three-dimensional data plot (not a simulation) of C_m vs. Φ and τ. The gold bar on the floor of this figure is discussed in Annex III.

3.8.5 Precision Material Removal

The holes made in target materials for low energy ablation shots were very precise. Figures 19a and 19b are, respectively, a blowup of the smallest spot in Figure 12, and a photomicrograph of the ablation feature produced on aluminized mylar. There may be applications for precise hole drilling based on this work.
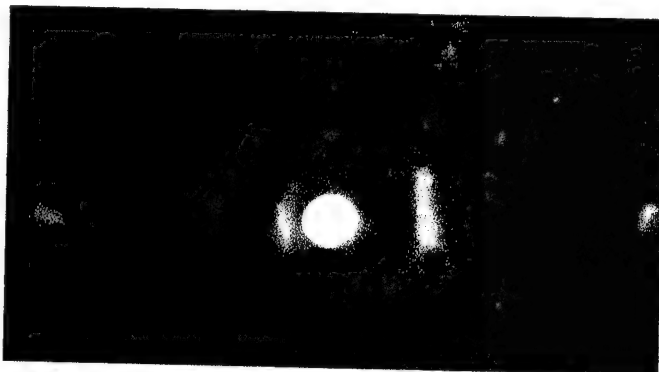
Figure 19a: Magnified view of smallest spot in Figure 12. Feature diameter is $20\mu m \pm 10\%$. Pulse duration 5ms.
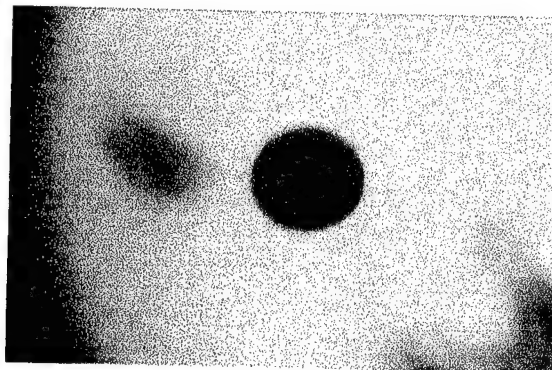
Figure 19b: $125\mu m$ kapton with aluminum flashcoat. Feature diameter is $180\mu m \pm 5\%$. Laser spot size $\tau=200ms$, $<\Phi>= 280J/cm^2$.

As a very interesting aside for our program, <u>thrust reversal</u> i.e. forward rather than backward thrust, was seen with aluminized kapton illuminated from the kapton side. This should be explored further during Phase II.

4. **Personnel. Publications, Inventions**

Personnel directly involved in the theoretical and experimental work for this project were:

Dr. Claude Phipps   Photonic Associates, Santa Fe, NM (PI for prime contractor)

Dr. James Luke   University of New Mexico, New Mexico Engineering Research Institute, Albuquerque, NM (PI for subcontractor)

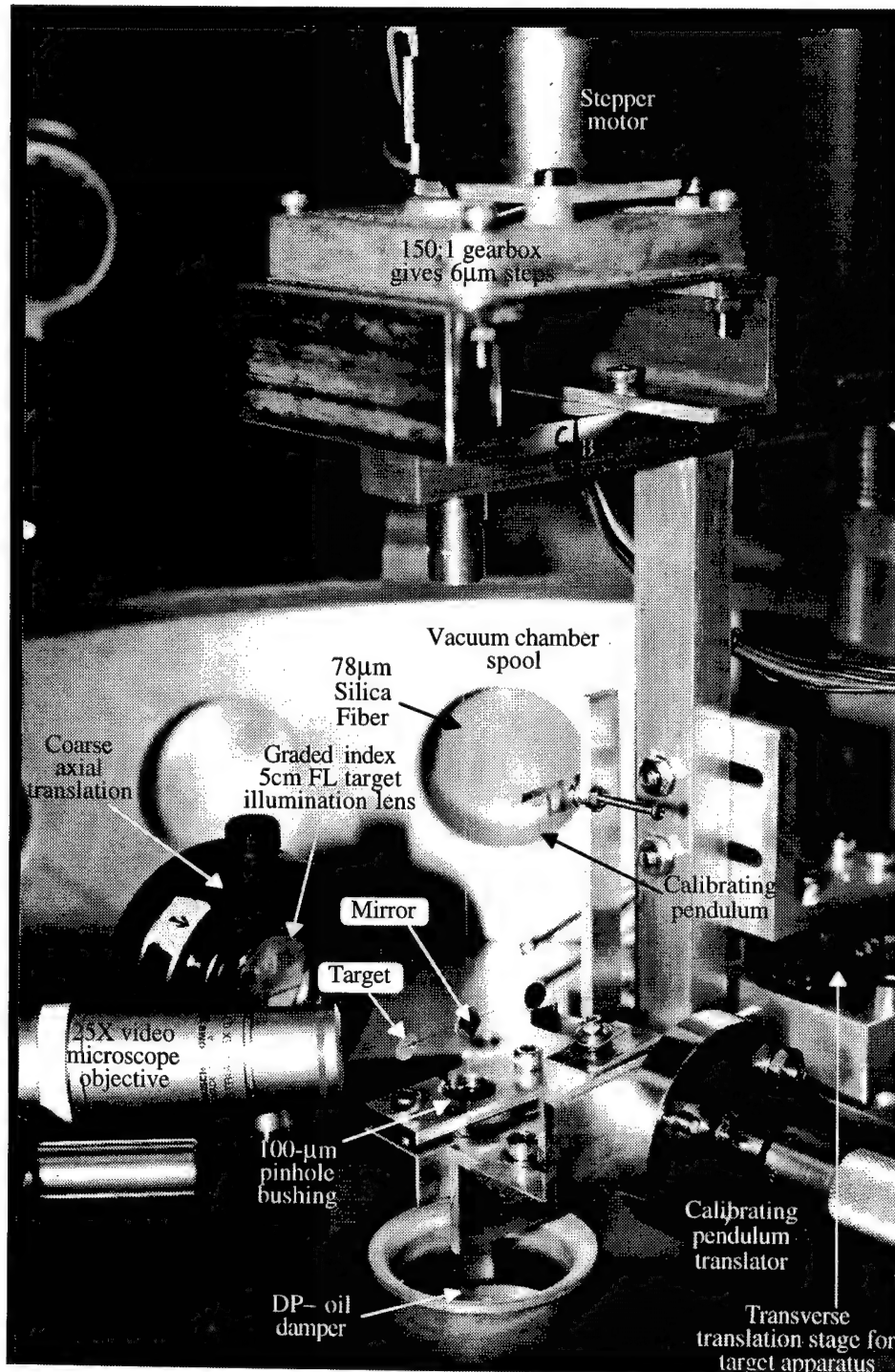**Publications:** None at this writing

Inventions: None. The University of New Mexico is conducting a prior art search in preparation for possibly filing a patent application on behalf of Photonic Associates and UNM, joint applicants. However, a decision on whether or not to file has not been made at this date.
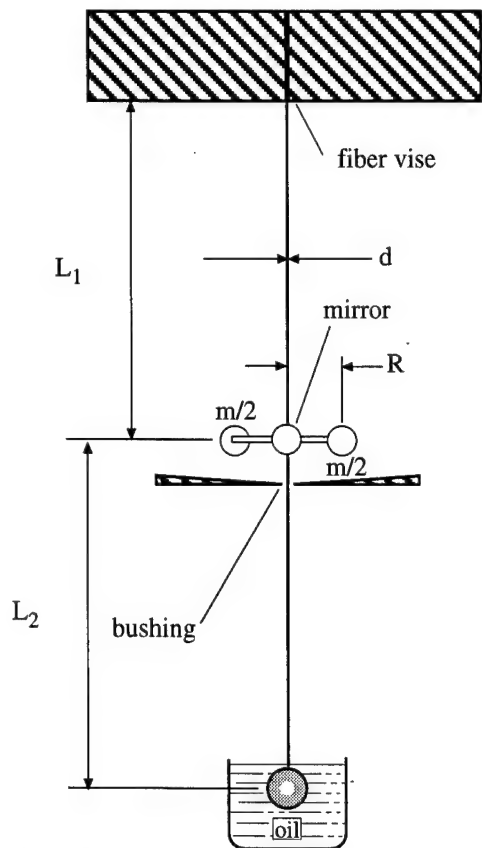
5. **References**

Phipps, C.R., ed. 1998 *Proc. SPIE High Power Laser Ablation Conference, Santa Fe* , SPIE Press 3343

Lang, R., O'Brien, S. Schoenfelder, A., Hagberg, M., Demars, S. and Li, B. 1998 "High Power, High Brightness Diode Lasers", *Proc. 1998 Diode Laser Technology Review, Albuquerque, NM*

Phipps, C.R. 1997 "Ultrashort Pulses for Impulse Generation in Laser Propulsion Applications", *Proc. Thirteenth International Conference on Laser Interactions and Related Plasma Phenomena, U.S. Naval Postgraduate School, Monterey, California*

Phipps, C.R., Friedman,H., Gavel,D., Murray, J.,Albrecht, G., George, E.V., Ho, C., Priedhorsky, W., Michaelis, M.M., and Reilly,J.P. 1996, "ORION: Clearing near-Earth space debris using a 20-kW, 530-nm, Earth-based, repetitively pulsed laser", *Laser and Particle Beams*, 14 (1) pp. 1-44

Phipps, C.R. 1996 in *Project ORION: Orbital Debris Removal Using Ground-Based Sensors and Lasers*, J. W. Campbell, ed. NASA Marshall Spaceflight Center Tech Memorandum 108522

Phipps, C.R. and Michaelis, M.M. 1994, "LISP,"*Laser and Particle Beams*,12 (1), 23-54

Phipps,C.R. and Dreyfus,R.W. 1993 "Laser ablation and plasma formation" in *Laser Ioni-zation Mass Analysis*, Akos Vertes,Renaat Gijbels & Fred Adams, eds.,Wiley,New York, 1993

Phipps, C. R. 1993a "Efficient Space Propulsion Engines Based on Laser Ablation," *Proceedings of the Los Alamos Technology Exchange Workshop, "Dynamic Response of Materials to Pulsed Heating," January 22-5*

Phipps, C.R. 1993b, "Modification of Earth-satellite orbits using medium-energy pulsed lasers," in *Proceedings of the Ninth International Symposium on Gas Flow and Chemcial Lasers, Crete, Greece,* C. Fotakis, C. Kalpouzos and T. Papazoglou, eds., SPIE volume 1810, SPIE, Bellingham, WA

Phipps, C.R. and Michaelis, M.M. 1992 "Space Propulsion Concept using High Energy, Pulsed Laser Ablation", *Proceedings of the Physics of Nuclear Induced Plasmas and Problems of Nuclear Pumped Lasers Conference, Obninsk, Russia*

Phipps, C.R., Harrison, R.F., Shimada,T.,York,G.W.,Turner,T.P.,Corlis,X.F., Steele, H.S., Haynes L.C. and King, T.R. 1990, "Enhanced Vacuum Laser-impulse Coupling by Volume Absorption at Infrared Wavelengths",*Laser and Particle Beams*, 8, 281

Phipps,C.R.,Turner,T.P.,Harrison,   R.F.,York,G.W.,Osborne,W.Z.,Anderson, G.K.,Corlis,X.F.,Haynes,L.C.,Steele,H.S.,Spicochi,K.C.,and   King,T.R.1988,   "Impulse Coupling to Targets in Vacuum by KrF, HF and CO_2 Lasers",*J. Appl. Phys.*, 64, 1083

Annex I: Phase I Torsion Microbalance – Theory and Calibration

We constructed one of the most sensitive pendula ever made [Figure AI.1]. The Figure shows the factors involved in the torsion pendulum's rotational response to laser-produced impulse. We are measuring material ablation pressure here, not light pressure. However, our pendulum is sufficiently sensitive to detect light pressure.

Figure AI.1: The torsion pendulum, under calibration

Figure AI.2: Parameters used in analysis

Table AI.1: Glossary

Symbol	Definition	Value or equivalence
C_m	Coupling coefficient	dyn-s/J
d	Fiber diameter	78±0.5 E-4 cm
E	Fiber Young's modulus	$7.08E11$ dyn/cm^2
f_o	Resonant frequency	Hz
F	Force	dyn
g	Acceleration of gravity	cm/s^2
G	Torsion modulus	$3.00E11$ dyn/cm^2
I	Rotating mass moment	(mR^2) gm-cm^2
J	Fiber polar moment	cm^4
k	Torsional spring constant	GJ/L
L	Effective fiber length	$[1/L_1+1/L_2]^{-1}$cm
m	Effective mass at radius R	gm
M	Torque	dyn-cm
n/m	not measured	
p	Impulse	dyn-s
θ	Rotation angle	rad
θ_b	Deflection angle of probe	rad
θ_o	Rotation amplitude	rad
R	Impulse moment arm	2 cm
σ	Fiber tensile strength	$5.39E8$ dyn/cm^2
T	Oscillation period	$(2\pi/\omega_o)$ s
W	Rotation kinetic energy	erg
W_L	Incident laser energy	J
ω_o	Resonant frequency	$2\pi f_o$ rad/s
z	Range to video recorder	cm

Torque defines the constant k:

$$M = F\,R = k\,\theta \qquad [AI.1]$$

$$k = \frac{G\,J}{L} \text{ , where} \qquad [AI.2]$$

$$J = \frac{\pi\,d^4}{32} \qquad . \qquad [AI.3]$$

Equating kinetic and stored energy,

$$W = \frac{k\,\theta_o^2}{2} = \frac{p^2}{2\,m} = \frac{I\,\omega_o^2\,\theta_o^2}{2} \qquad [AI.4]$$

gives the resonant frequency,

$$\omega_o = \sqrt{\frac{k}{I}} \qquad . \qquad [AI.5]$$

From [AI.4], the impulse response of the pendulum is:

$$\frac{p}{\theta_o} = \sqrt{k\,m} = \sqrt{\frac{G\,J\,m}{L}} = \sqrt{\frac{\pi\,G\,m}{32\,L}\,d^2} \qquad \text{, and} \qquad [AI.6]$$

$$\frac{F}{\theta_o} = \frac{G\,J}{L\,R} \qquad [AI.7]$$

is the force response.

These relationships suggest four distinct ways of determining the precise value of the product GJ by either calibration or direct calculation:

From Eq. [AI.3] by observing the resonant frequency of i =1,2 (light, heavy) pendulum and calculating the effective rotating mass:

$$(GJ)_{1i} = L_i m_i R^2 \omega_{oi}^2 \qquad [AI.8a]$$

or, by direct calculation based on tabulated material constants for our 78μm diameter fused silica fiber:

$$(GJ)_2 = \frac{\pi d^4 G}{32} = 109.0 \qquad [AI.8b]$$

or, by applying a known <u>force</u> from a standard pendulum and observing the deflection θ:

$$(GJ)_{3i} = \frac{F_i L_i R}{\theta_i} \qquad [AI.8c]$$

or by applying a known <u>impulse</u> via a collision from a standard pendulum and observing the deflection amplitude:

$$(GJ)_{4i} = \frac{p^2 L_i}{m_i \theta_{oi}^2} \qquad [AI.8d]$$

Of these, method 3 proved by far the most successful in generating a precise result. With method 4, finding the correct coefficient of restitution for zero recoil of the test mass was very difficult, and accurately measuring the recoil was difficult. In contrast, with method 3, the measured variables were simple and static, giving a measurement accuracy better than 5% [Figure AI.3].
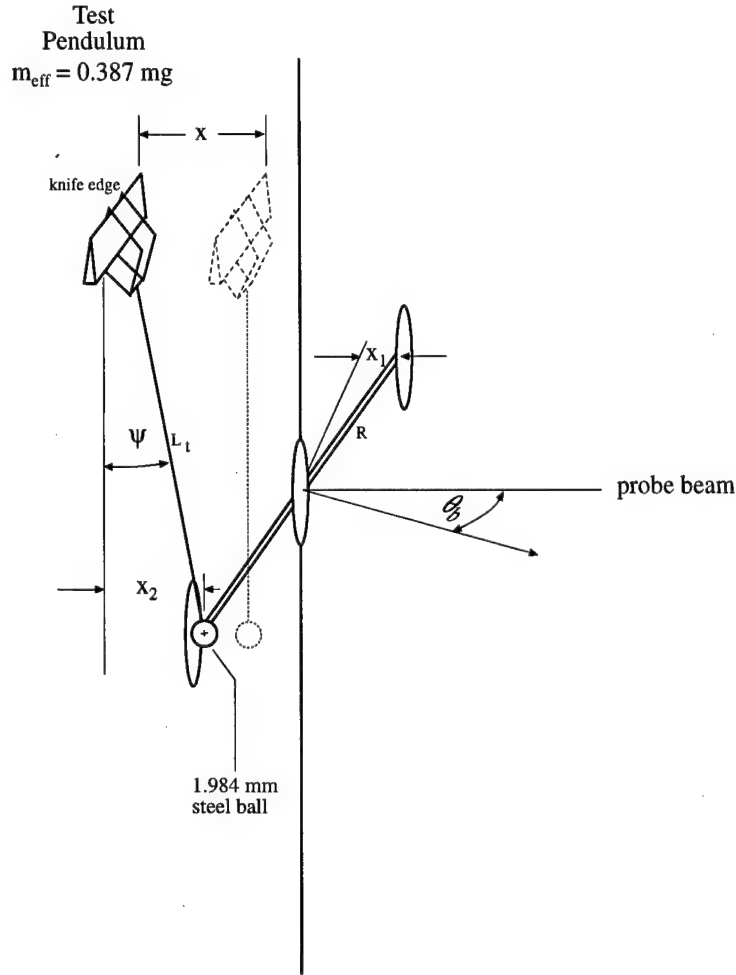
Given an accurate value for k, what is ultimately desired, of course, is the momentum coupling coefficient C_m [which is universally tabulated in the literature in mixed units (dyn-s/J)]:

$$C_m = (p/\theta_o)(\theta_o/W_L) \qquad . \qquad [AI.9]$$

The angles θ are evaluated by reflecting a probe laser off a
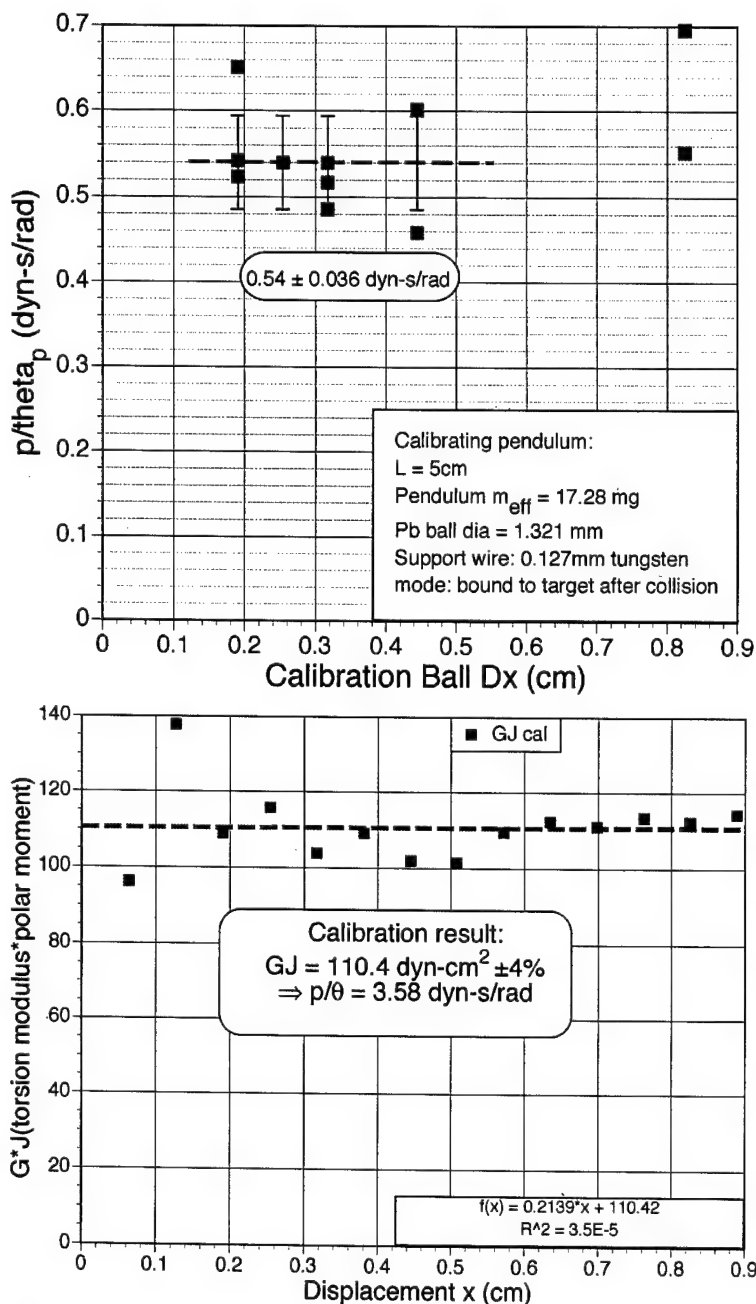
Figure AI.3: **Impact calibration (upper) was much less accurate than static force calibration (lower figure)**

Test
Pendulum
$m_{eff} = 0.387$ mg

Figure AI.4: Static force calibration setup

micromirror mounted to the center of the torsion mechanism [Figures AI.1, 2]. The force calibration is illustrated in Figure AI.4. It is necessary to take account of the fact that both pendula move when the test pendulum is advanced a distance x via a micrometer stage. We have

$$x_2 = x - x_1 \qquad [AI.9]$$

$$F_2 = m_{eff} \, g \tan \psi \qquad \text{and} \quad [AI.9]$$

$$GJ = \frac{2 F_2 R L}{\theta_b} \qquad [AI.10]$$

from Eq. [AI.8c] with $\theta_i = \theta_b/2$. This simple method resulted in the precise data shown in Fig. AI.3 (lower). We note [Table AI.1] that the value for GJ agrees very well (within 1%) with the calculated value $(GJ)_2$.

The more customary alternative of calibration via impact of a test pendulum was relatively inaccurate. We could not achieve zero coefficient of restitution in the test mass, and resonances in both structures made it difficult to accurately determine the test mass rebound. We then settled on making the test mass stick to the torsion pendulum - a case easier to analyze - but then, the Q of the coupled pendulum oscillation was very low, and the correction for damping was consequently inaccurate.

Summary: In practical terms, then, using the best values in Table AI.1, we have:

$$\frac{F}{\theta} = \binom{13.40}{11.04} \text{dyn / rad} \quad \text{for the} \ \binom{\text{light}}{\text{heavy}} \quad \text{pendulum, respectively,} \quad [AI.11a]$$

and $\quad \dfrac{p}{\theta} = \binom{0.681}{3.58} \text{dyn} - \text{s / rad} \ \ \text{for the} \ \binom{\text{light}}{\text{heavy}} \quad \text{pendulum,} \quad [AI.11b]$

as indicated in the Table. The items in the last column of Table AI.1 differ because the effective lengths L_i of the two pendula differ.

Table AI.1: Calibration Results for the Torsion Pendula

Pend.	Freq. f_o(Hz)	Mass m(mg)	L_1 (cm)	L_2 (cm)	$(GJ)_1$	$(GJ)_2$	$(GJ)_3$	$(GJ)_4$	Final p/θ (dyn-s/rad)	Final F/θ (dyn/rad)
Light	1.73	17.28	10	7	33.64	109.0	n/m	69.53	0.681±4%	13.40
Heavy	0.333	579.6	10	10	50.75	109.0	110.4	n/m	3.58±4%	11.04

Recording Setup

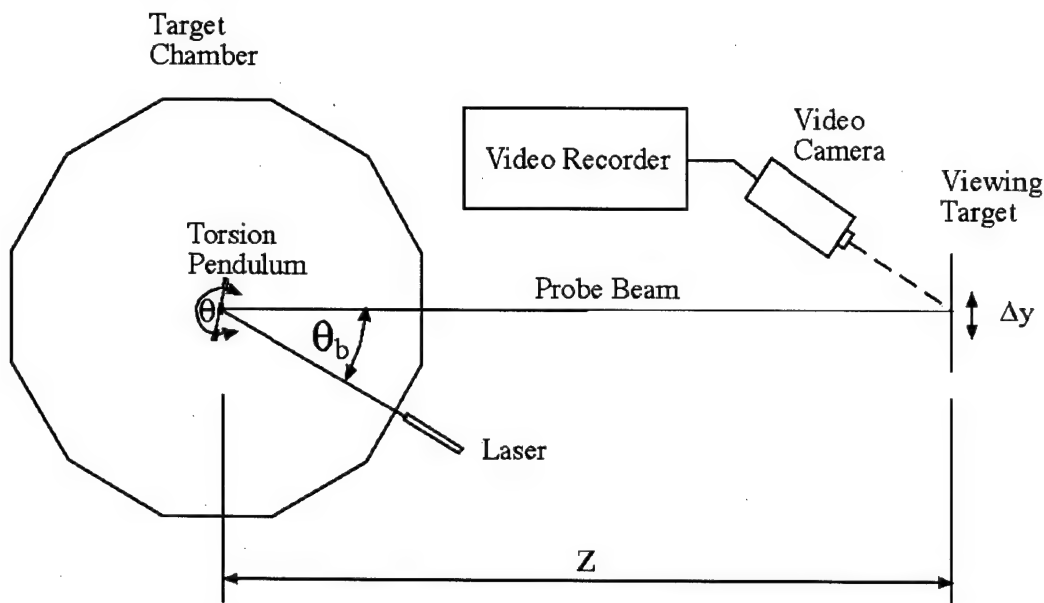Figure AI.5 shows the recording setup.

Figure AI.5. The Impulse Recording Setup

Sensitivity

Keeping in mind that reflection of the probe beam θ_b from the microbalance mirror doubles the rotation angle of the balance θ:

$$\theta_b = 2\theta \qquad [AI.12]$$

the sensitivity of the final device simply depends on the minimum deflection amplitude Δy we can read and the range z to the target on which the video system records this reading:

$$\theta_{b\ min} = \Delta y/z \qquad . \qquad [AI.13]$$

We used two ranges, which are listed, together with corresponding sensitivity at ±50% in Table AI.2.

Table AI.2: Pendulum Sensitivity at ±50% Accuracy [Δy_{min} = 0.1 mm]

Pend.	p/θ (dyn-s/rad)	$\Delta\theta_{min}$ @ z=340 cm (μrad)	$\Delta\theta_{min}$ @ z=23.5 cm (μrad)	Δp_{min}: @ z = 340 cm (dyne-s)	Δp_{min}: @ z = 23.5 cm (dyne-s)
Light	0.681	14.7	213	1.00E-5	1.45E-4
Heavy	3.58	14.7	213	5.26E-5	7.63E-4

Maximum response as presently configured occurs with the heavy pendulum, z=23.5 cm and Δy_{max} = 25 cm, giving Δp_{max} = 1.90 dyne-s.

Measuring Light Pressure

The effective coupling coefficient for reflection of light (with no ablation) is

$$C_m = 2/c \text{ in consistent units or}$$

$$= 6.7E\text{-}4 \text{ dyne-s/J in customary units} \qquad [AI.14]$$

[Phipps, *et al.* 1988]. If we apply our laser to a reflecting target on the light pendulum in its maximum sensitivity configuration (z=340 cm) without a focusing lens, at intensities of order 0.5 W/cm^2, any deflection seen will be due to light pressure, not ablation.

We did this on the final day of our experimental program and were able to see light pressure quite well.

The target was aluminized mylar, 1cm x 5mm. Maximum cw intensity on the target was 700mW/cm^2 (about 7 suns) and maximum pulse fluence was 300mJ/cm^2. With a maximum pulse duration of 150ms in the test, we obtained deflection (in the correct direction) of 15 times the minimum measurable respnse. We were still able to see light pressure deflection down to 10ms.

Chamber pressure was 1.6E-4 torr.

Annex II: Target Matrix [objective h]

Table AII.1. Test Summary

Test Nos	Target	d_s (µm)	t (µm)	Pend. Lt	Pend. Hvy	Pulse width Min (ms)	Pulse width Max (ms)	Fluence Min J/cm^2	Fluence Max J/cm^2	C_m (d-s/J)	Q^* (J/g)	I_{sp} (s)	Impulse (bits) Min	Impulse (bits) Max	Log Ratio[1]
4,12	Black printer's ink:paper	5	350	X		0.1	40	65	1.70E+3	15	1.6E5	2000	1	1740	
30	Black printer's ink:paper	5	350		X	100	300	64	3.12E3	5.9	---	---		6400	
6	Black printer's ink:paper	100	350	X		0.8	60	3.7	3.40E+2	10	2.3E5	830	14	2170	
17	Black printer's ink:paper	200	350	X		0.2	50	9.1	4.30E+1	2.8	---	---	7	300	
21,22	Black printer's ink:paper	200	350		X	10	300	11	3.64E+2	8.8	3.3E4	180	114	9370	3.97
9,16	Xerographic black:paper	5	100	X		0.1	80	32	4.64E+3	8.1	9.7E4	135	2	2320	
24	Xerographic black:paper	200	100		X	5	300	5.7	1.50E+2	9.5	3.3E4	230	76	5260	3.42
41,46	Thin PVC film	5	175	X		0.1	5	850	3.55E+3	21	1.6E5	350	1	370	
37	Thin PVC film	5	175		X	1	300	320	8.55E+3	12	3.4E4	505	38	1.6E4	
38	Thin PVC film	200	175		X	2	300	5.7	8.90E+1	24	4930	72	12	1840	
44	Thick PVC film	5	500	X		0.1	20	80	2.20E+3	20	4.4E5	465	12	1840	4.20
8	Phenolic resin	5	250	X		0.8	100	615	5.56E+3	10	---	---	29	1930	
29	Phenolic resin	5	250		X	2	300	640	---	5.7	---	---	38	5640	
31	Phenolic resin	200	250		X	10	300	11	1.53E+2	6.4	8840	43	12	1840	2.67
47,48	Black ink: mylar	5	50	X		0.05	1	19	3.13E+2	8.4	7.0E4	330	0.75	22	
23	Black ink: mylar	200	50		X	2	300	2.3	2.30E+2	6.4	2.9E4	72	12	1840	3.39

Test Nos	Target	d_s (μm)	t (μm)	Pend. Lt	Pend. Hvy	Pulse width Min (ms)	Pulse width Max (ms)	Fluence Min J/cm²	Fluence Max J/cm²	C_m (d-s/J)	Q^* (J/g)	I_{sp} (s)	Impulse Min	Impulse Max	Log Ratio[1]
25	Black ink: mylar sandwich	200	100		X	---	300	---	2.30E+2	---	---	---	---	---	---
43	Black ink:glass[2]	5	90	X		0.1	20	32	1.35E+3	22	2.6E4	311	3.6	556	
42	Black ink:glass	100	90	X		0.1	20	0.9	4.70E+1	16	1.4E4	132	3.6	674	2.27
32	Black thin polyethylene	5	100		X	5	300	1600	6.50E+4	0.21	1.7E4	1.5	15	76	
34	Black thick polyethylene	5	850		X	50	300	1.4E4	2.00E+4	1.5	2600	3.6	150	1500	2.00
45	Kapton	5	125	X		0.2	200	320	6.50E+3	---	---	---	---	---	---
13	Photographic film	5	175	X		0.1	60	16	8.54E+3	7.4	1.7E4	97	0.5	72	2.16
18	Audio tape	5	50	X		0.1	80	95	7.90E+3	6.7	1.2E5	300	3.6	145	
19,20	Audio tape	200	50	X	X	8	300	9.2	3.00E+2	2.6	3.3E4	15	57	380	2.02
26	Graphite sheet	5	380		X	100	300	6600	2.00E+4	---	---	---	---	---	---
40	Viton	5	300		X	1	300	8060	4.80E+4	10.6	3.3E4	227	12	563	1.69
10	Se black:Al	5	100	X		0.8	80	380	4.05E+4	---	---	---	---	---	---
11	Black ink:vinyl copolymer	5	25	X		0.8	80	3140	4.05E+4	6.0	---	---	44	58	0.12
33	Cellulose nitrate	5	70		X	2	300	950	9.24E+4	---	---	---	---	---	---
39	Black anodize:Al	5	500		X	2	300	950	9.24E+4	---	---	---	---	---	---
36	Fiberglas	5	1500		X	2	300	950	9.24E+4	---	---	---	---	---	---

Notes:
1) For the material, independent of the spot size or the balance used to measure impulse
2) Same ink as expt. 23, dissolved and applied to glass cover slide in a thick layer
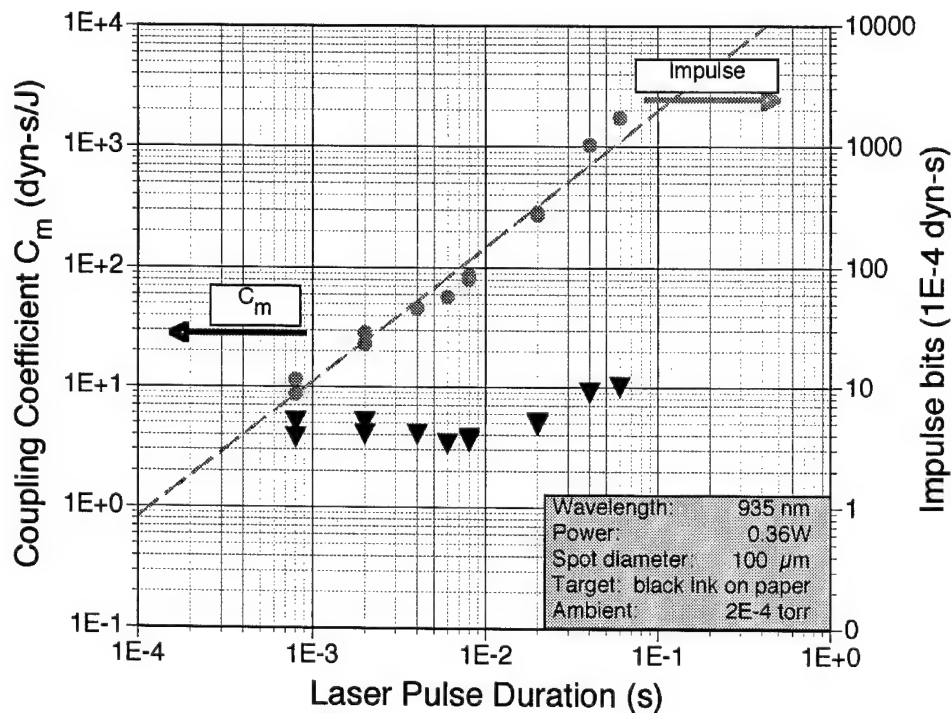3) Constant factors: Incident power 360mW, p<1mtorr

ID4,12&30: Black ink on paper, d_s = 5.2 μm
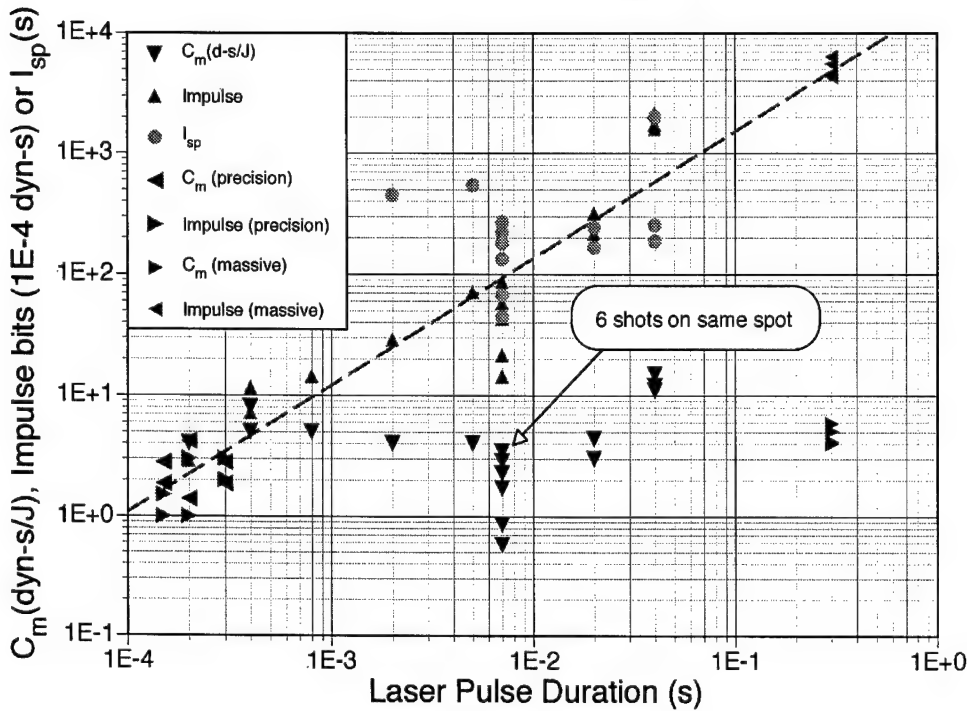
Figure AII.1 [ID4,12]

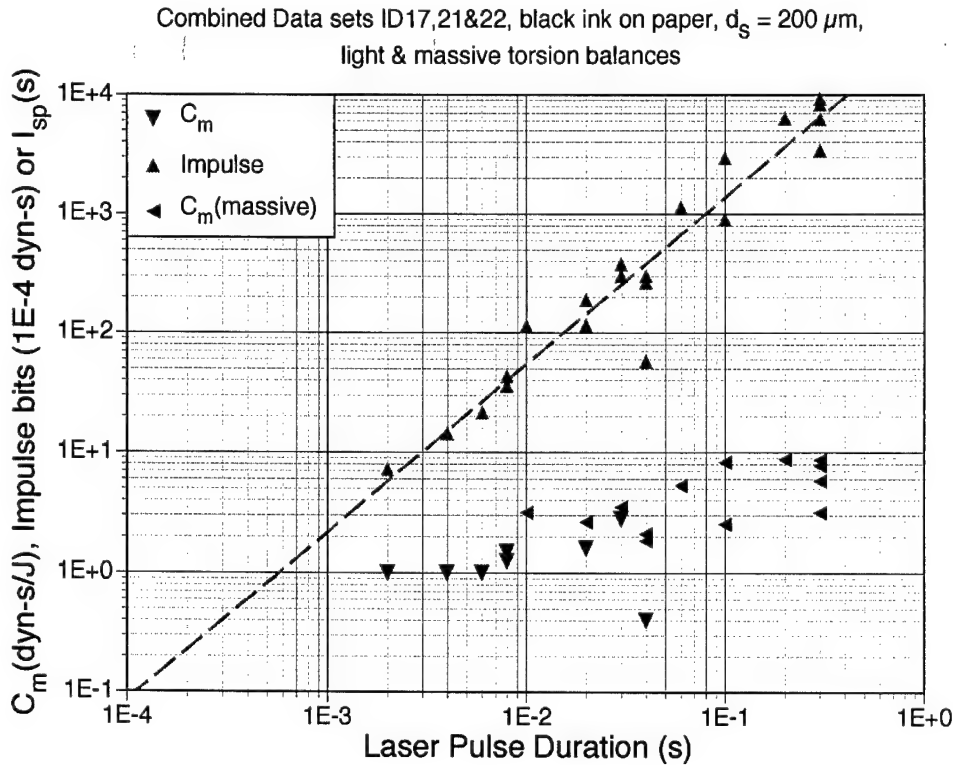**Black printer's ink on 350-μm paper substrate, 5μm spot**

Same as Figure 16 of main text. The multiple-shot data point shows how gracefully the thrust from a single point degrades. Data such as this created the 3-dimensional Figure 18 of the maint text.

Figure AII.2 [ID6]

**Black printer's ink on paper, as Figure AII.1 but 100-μm spot.**

No significant difference in coupling is seen.

Combined Data sets ID17,21&22, black ink on paper, d_S = 200 μm, light & massive torsion balances

Figure AII.3 [ID17,21&22]

Black printer's ink on paper, same as previous two Figures, but 200μm spot.

Still no significant difference in coupling from the smaller spots.

ID9, Laser print on bond, d_S = 5.2 μm
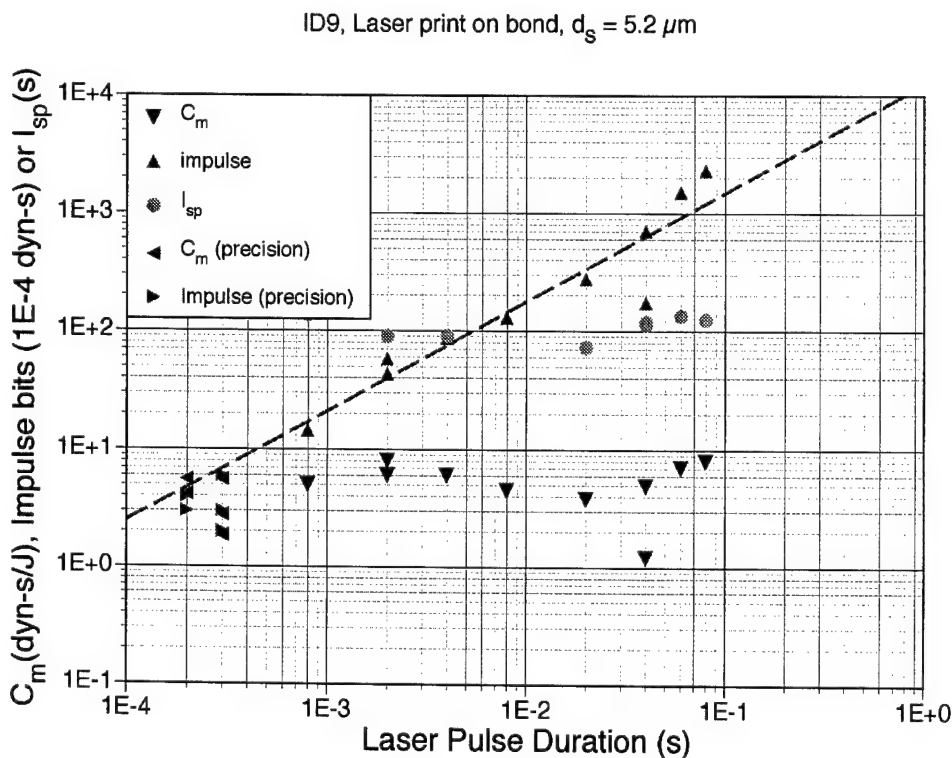
Figure AII.4 [ID9,16]

Laser print on white bond paper, 5μm spot

Laser print on bond paper gave good C_m, but not very exciting I_{sp}.

ID24, laser print, d_S =200μm
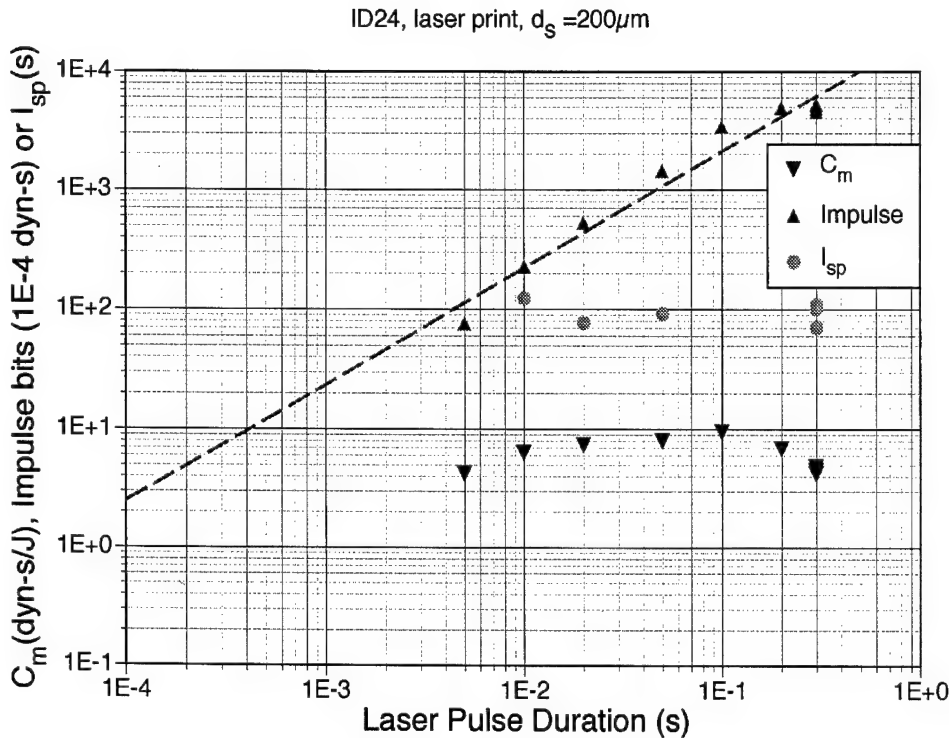
Figure AII.5 [ID24]

Laser print on white bond paper, same as previous figure but 200μm spot

Notice the expected improvement relative to the previous figure in coupling for longer pulses by using the larger illumination diameter. By ablating material from a larger area, burnthrough is delayed.

ID8&29, SiC 280 grit paper, d_S = 5.2 μm
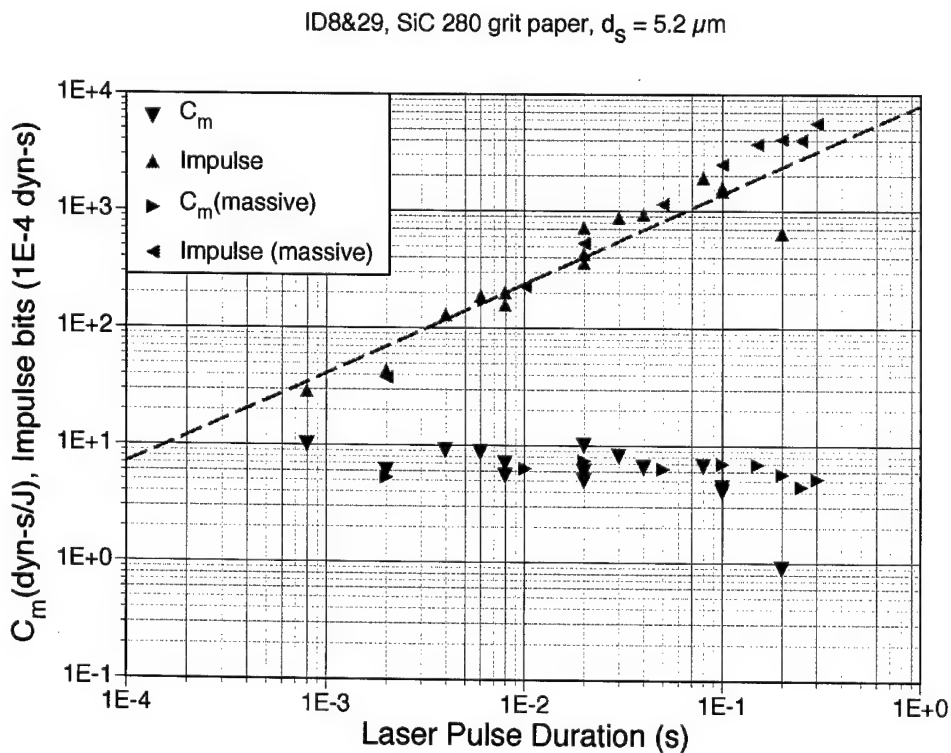
Figire AII.6 [ID8,29]

Phenolic Resin, 5μm spot.

The 280-grit paper gave our second-highest coupling coefficient. It is the binder, rather than the grit, that is providing the ablation. 3-M Corp was unable to identify the composition of the binder, other than "phenolic resin". Because ablation made blisters rather than cavities, we were unable to determine Q*.
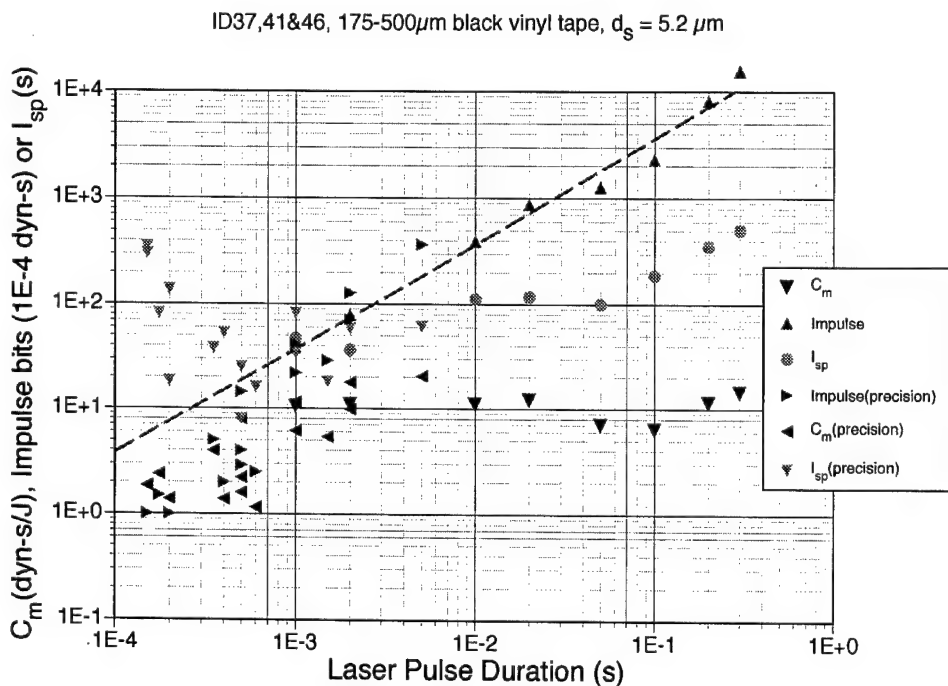
ID37,41&46, 175-500μm black vinyl tape, d_s = 5.2 μm
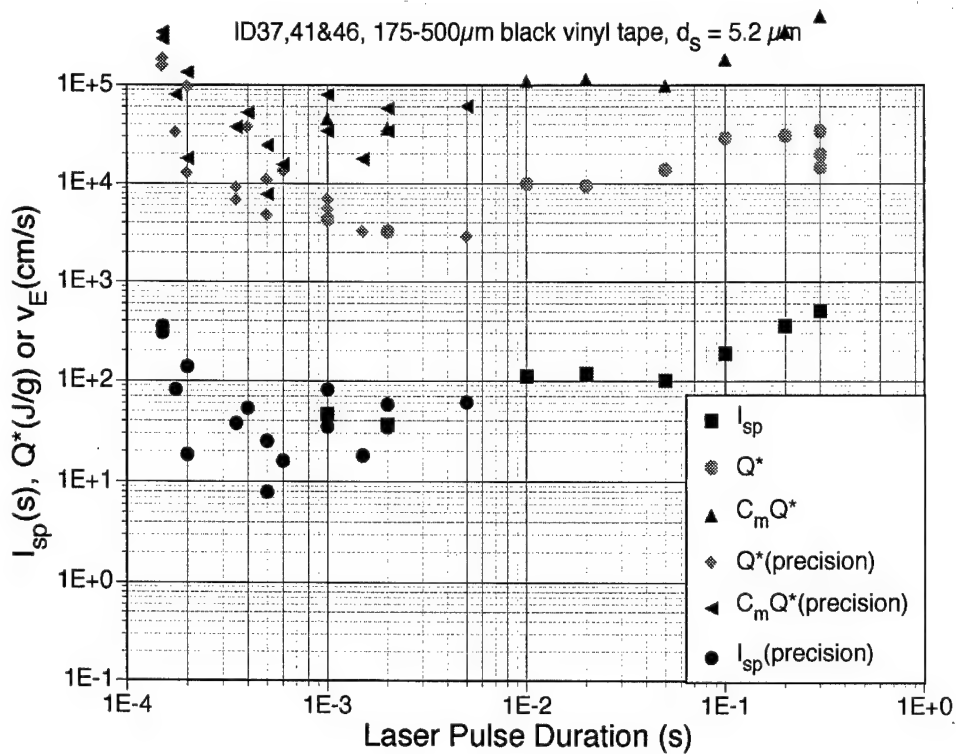
Figure AII.7 [ID37,41 & 46]

Q* data for black PVC film, 175-500μm thick, 5μm spot

This data matches the C_m plot immediately following.

I_{sp} values are relatively high.


ID37,41&46, 175-500μm black vinyl tape, d_s = 5.2 μm

Figure AII.8 [ID37,41 & 46]

C_m data for black PVC film, 175-500μm thick, 5μm spot

Same data as Figure 14 of the main text. Note how as fluence (proportional to pulsewidth) increases, coupling at first decreases because of localized burnthrough, then becomes indistinguishable from data [Figure AII.8] for a 200μm spot because of the "wings" on the laser's spacial irradiance distribution.

28

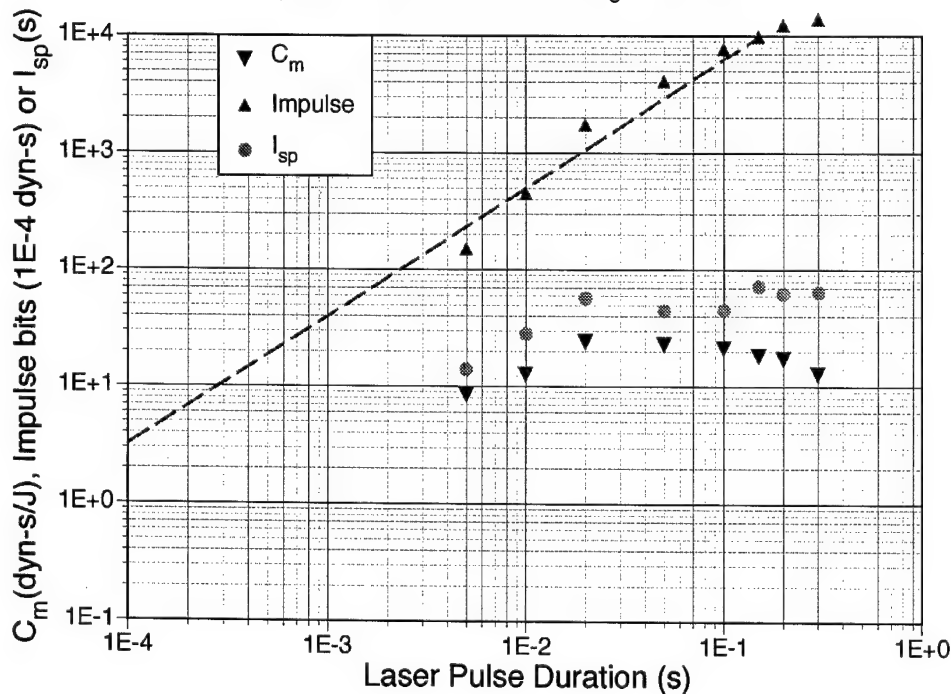ID38, 175µm black vinyl tape, $d_s = 200 \mu m$
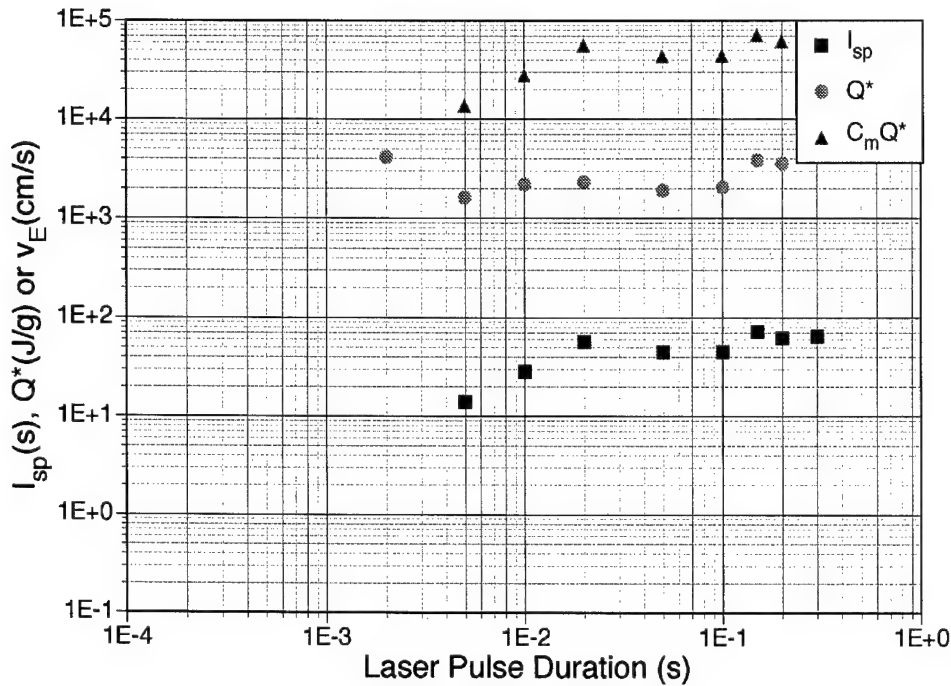
Figure AII.9 [ID 38] Q* data for black PVC film, 175µm thick with 200µm spot.
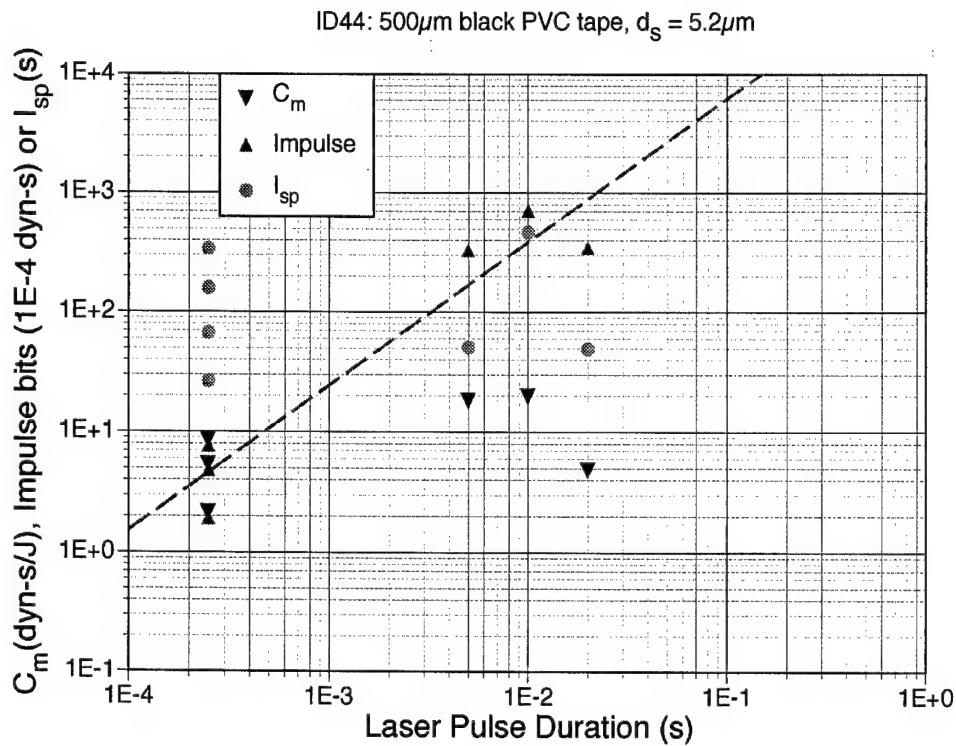
I_{sp} values are quite low with the larger spo size.

ID38, 175µm black vinyl tape, $d_s = 200 \mu m$

Figure AII.10 [ID38] C_m data for black PVC film, 175µm thick with 200µm spot.

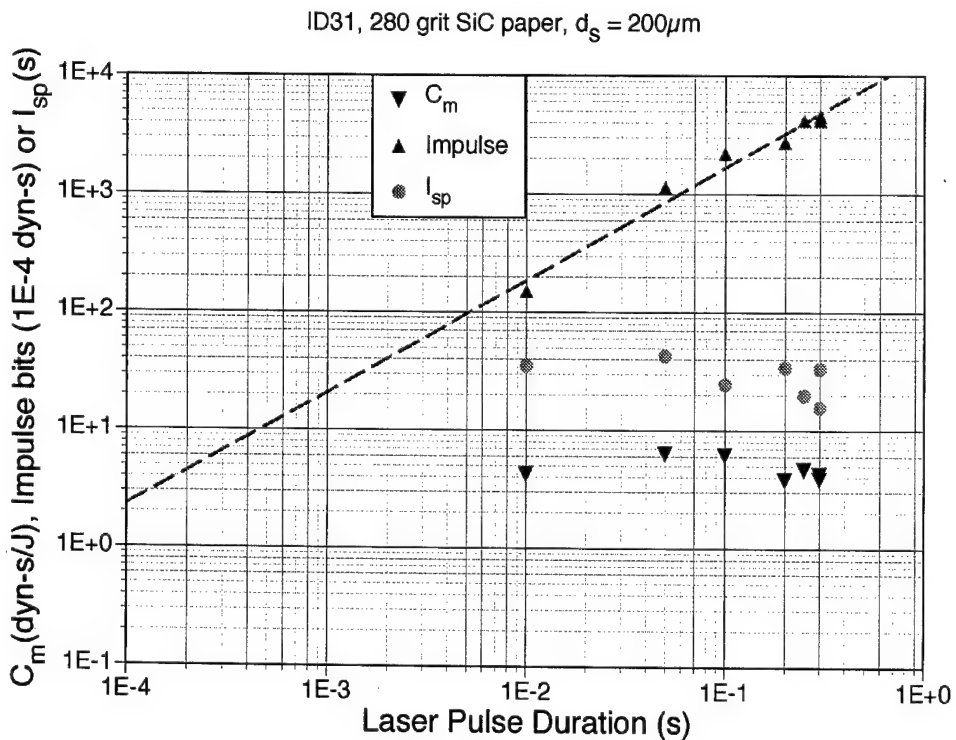Coupling coefficient is the largest we saw in the test series, but Q* and I_{sp} are low.

ID44: 500μm black PVC tape, d_s = 5.2μm

Figure AII.11 [ID44]

500-μm thick PVC film, 5μm spot.

Again, large C_m but modest Q^*.

ID31, 280 grit SiC paper, d_s = 200μm

Figure AII.12[ID31] Phenolic resin, same as Figure AII.6 but 200μm spot.

Lower coupling, poor I_{sp}.

ID47&48: 10μm typewriter tape, d$_S$ = 5.2μm
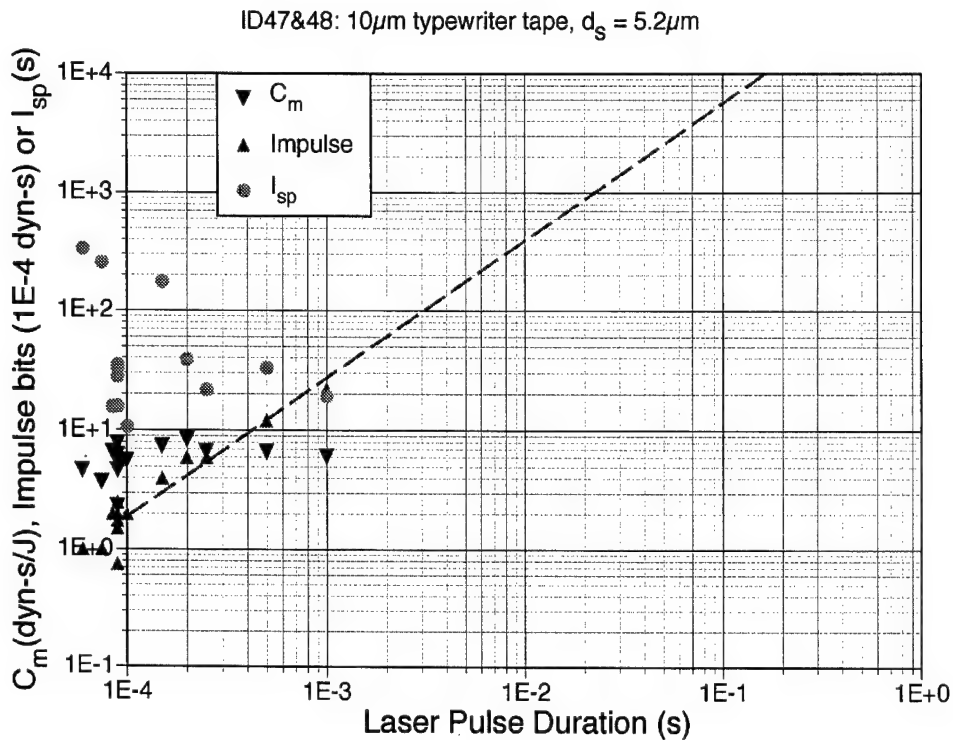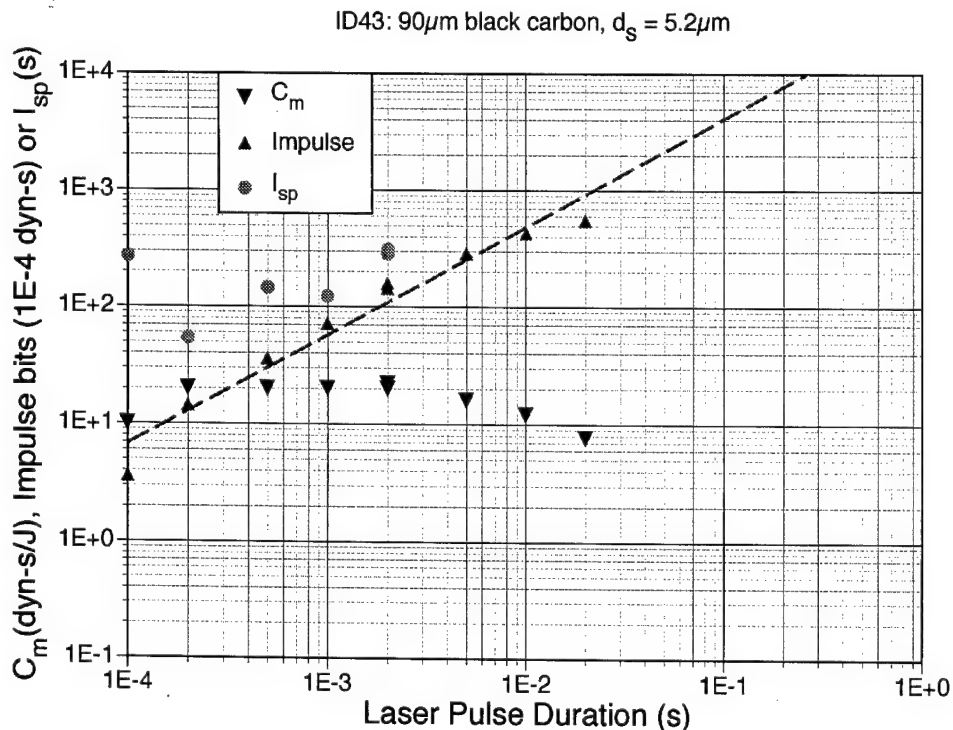

**Figure AII.13
[ID47&48]**

Black ink coating (est. 2μm) on 10μm mylar film substrate, 5μm spot.

Same data as Figure 17 of main text.

I_{sp} is the best we observed for 100μs pulses on any target.

ID43: 90μm black carbon, d$_S$ = 5.2μm

Figure AII.14 [ID48]

Thick black ink coating (90μm) on glass substrate, 5μm spot.

We dissolved the ink from the material in Figure AII.13 and applied it as a thick paste to see how coupling would survive for longer pulses. As expected, we got very good coupling near 1ms pulsewidth. I_{sp} was disappointing.

Compare Figure AII.18.
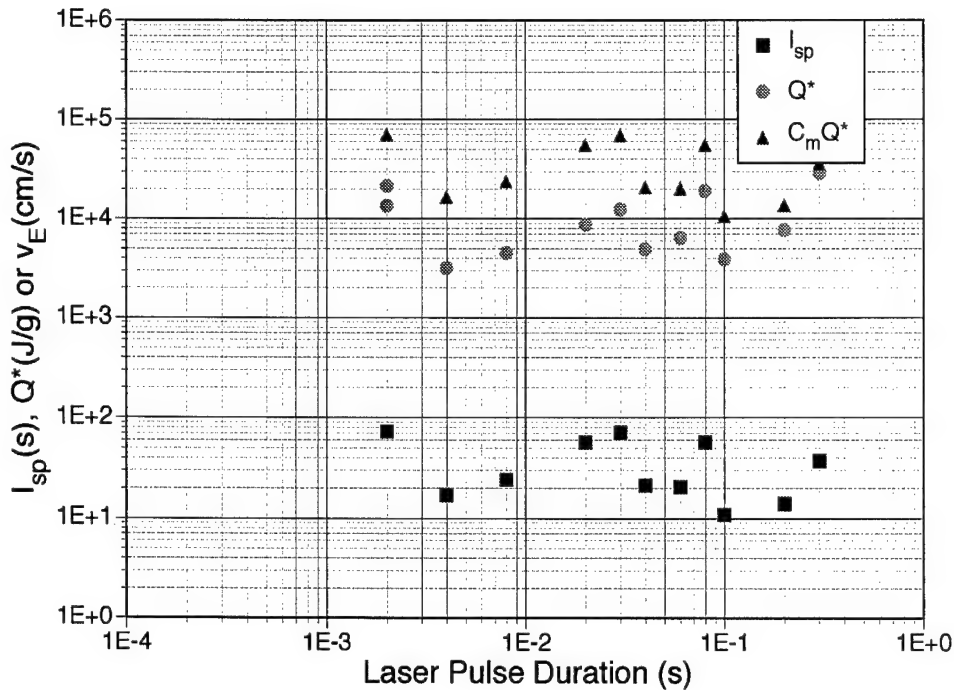
Data set ID23: typewriter tape at 200μm spot size

Figure AII.15 [ID23]

Q* data for black ink on mylar film, 200μm spot.

As expected, I_{sp} is very poor with the larger spot and the very thin absorbing coating.

ID23, typewriter tape, $d_S = 200 \mu m$

Figure AII.16 [ID23]
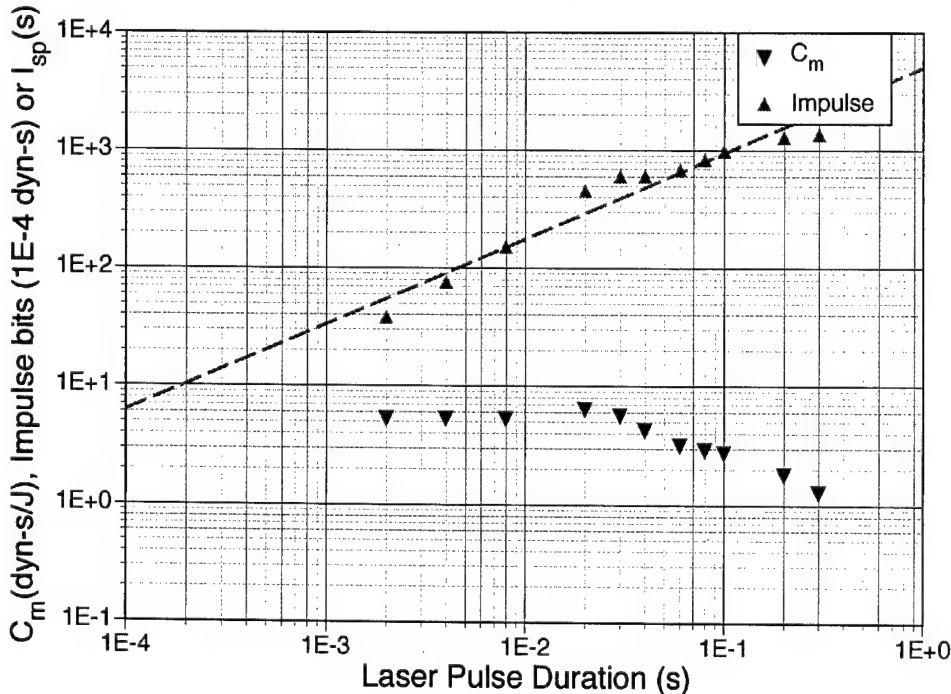
C_m data for black ink on mylar film, 200μm spot.

This is an excellent target for short pulses and small impulses. It is essentially the same material as Figure 15 of the main report.

This is a classic case of rapidly degrading coupling with increasing pulse duration because a thin absorbing coating (5-10μm) overlies either a highly transparent substrate. Burnthrough occurs at 10ms.

ID42: 90μm black carbon on glass, $d_S = 100μm$
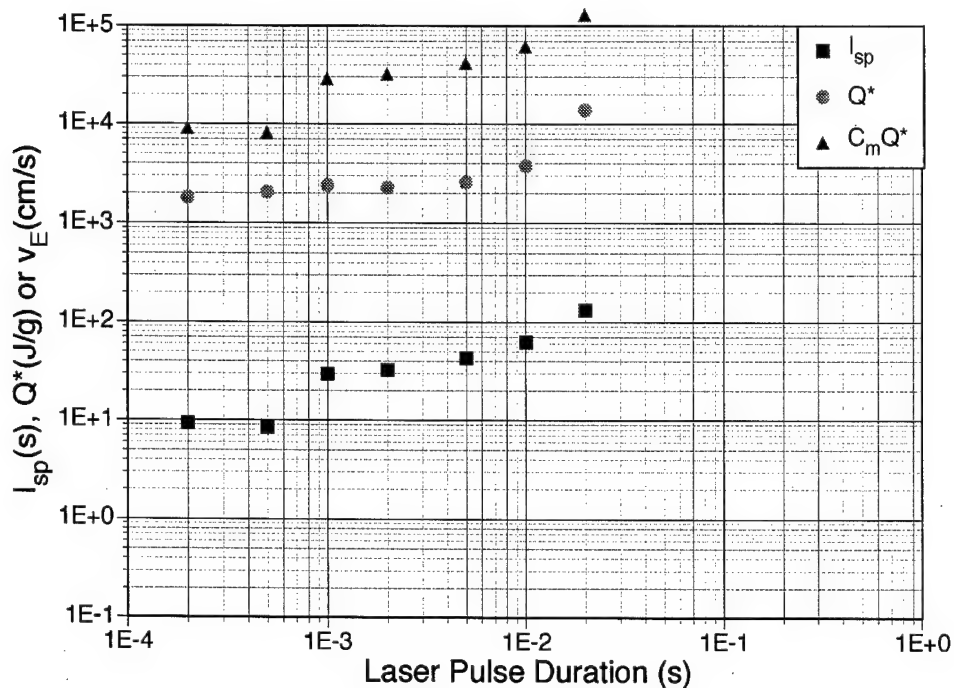
Figure AII.17 [ID42]

Q* data for 90μm-thick ink coating on glass, same target as Figure AII.14 but 100μm spot.

Uninspiring I_{sp} values are seen.

ID42: 90μm black carbon on glass, $d_S = 100μm$
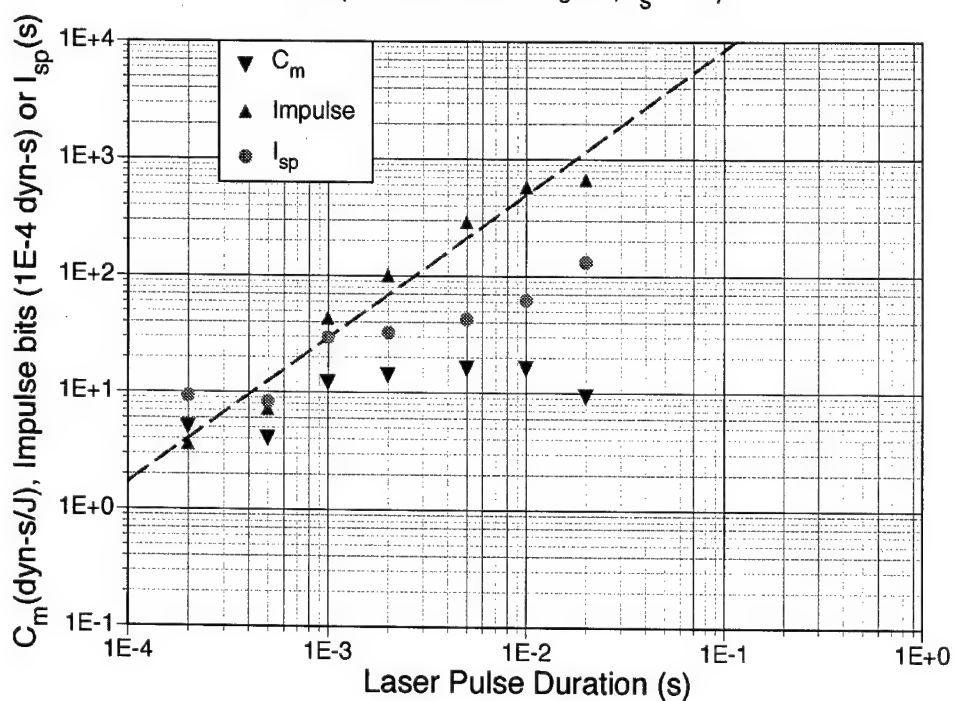
Figure AII.18 [ID42]

C_m data for 90μm-thick ink coating on glass, same target as Figure AII.17.

As expected, coupling peaks at 10ms rather than 1ms [see figure AII.14] because of the larger illumination spot. Good coupling, poor I_{sp}.

ID32, 100μm black poly, d$_s$ =5.2μm
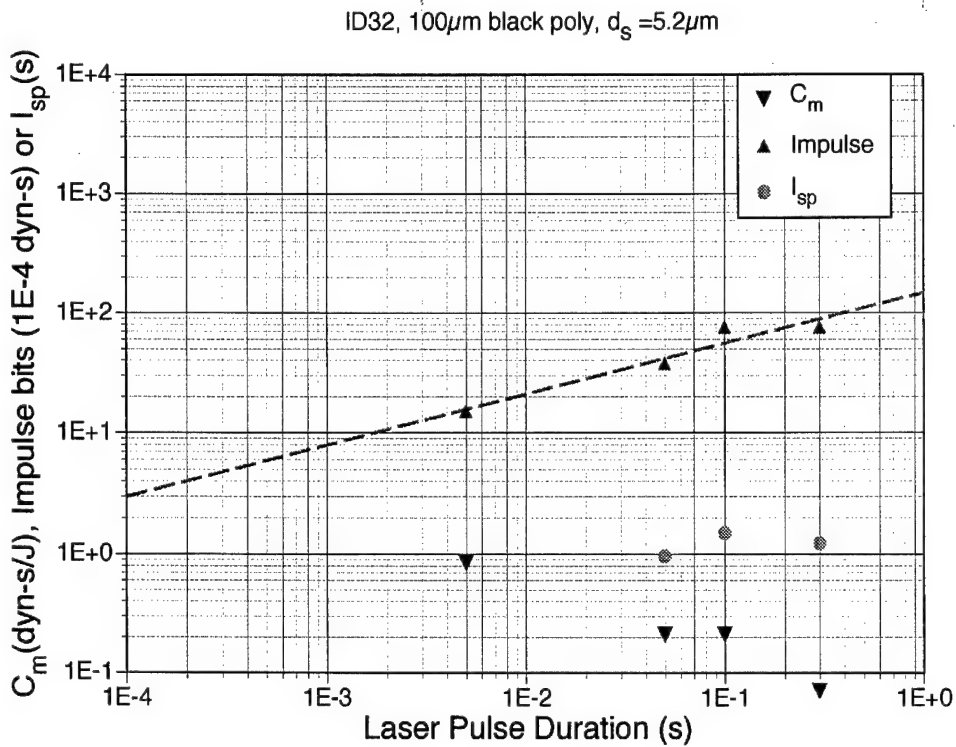
Figure AII.19 [ID32]

100μm thick black polyethylene

This data and that following shows that some materials will not couple well at the intensities we have available, even if they are highly absorptive.

ID34, 850um black poly (Kodak film can), d$_s$ =5.2μm
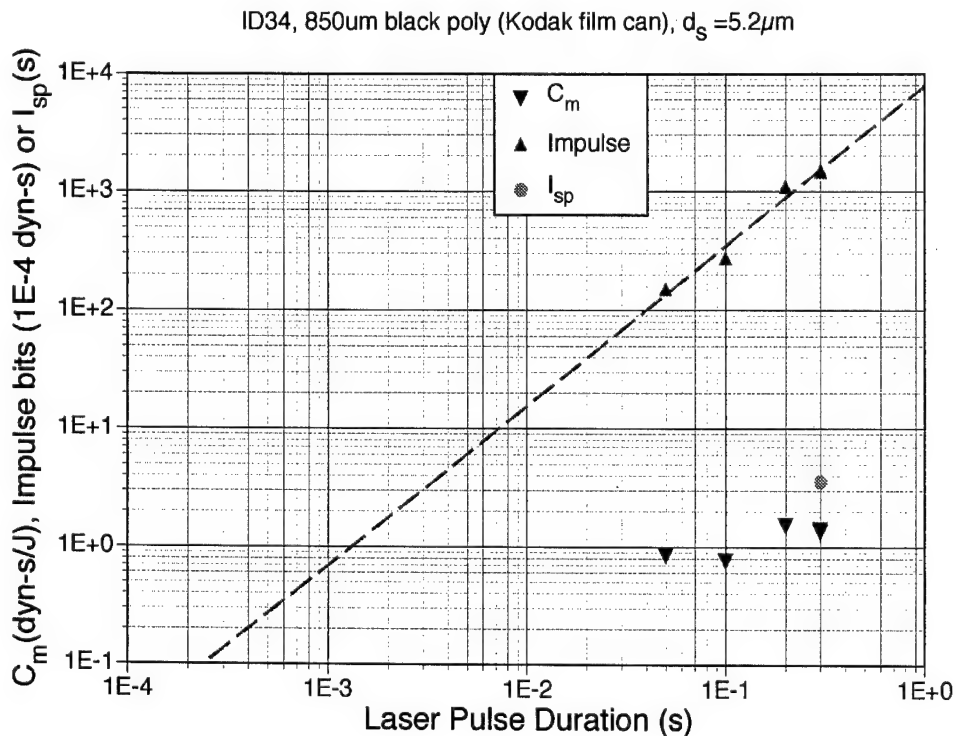
Figure AII.20 [ID34]

Thick (850μm) black polyethylene

34

ID13, color film at focus, d_S = 5.2μm
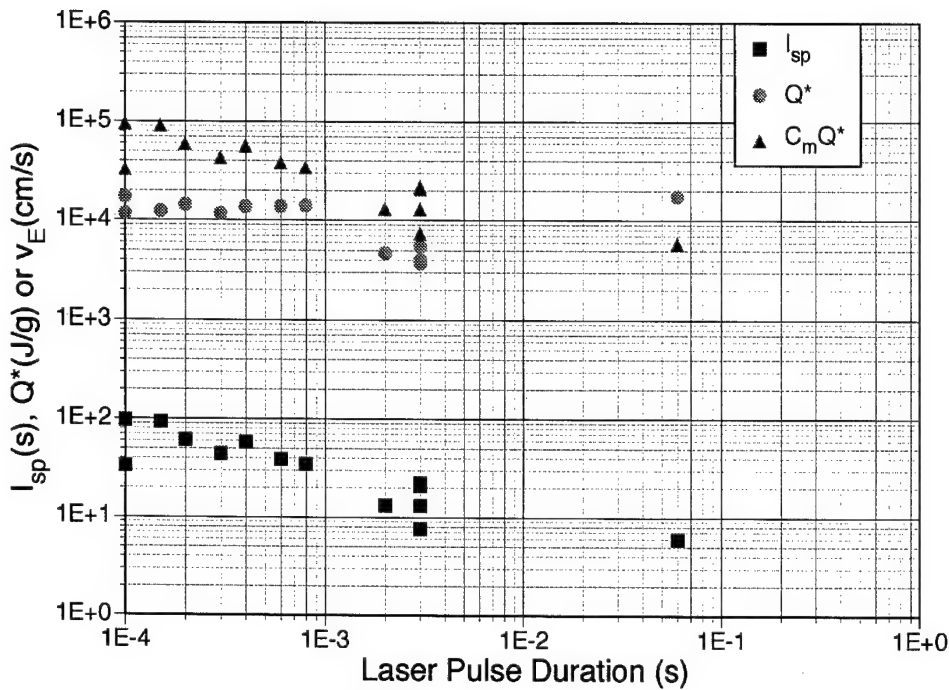
Figure AII.21 [ID13]

Q* data for undeveloped color film, emulsion side up, 5μm spot

ID13, color film, d_S = 5.2 μm
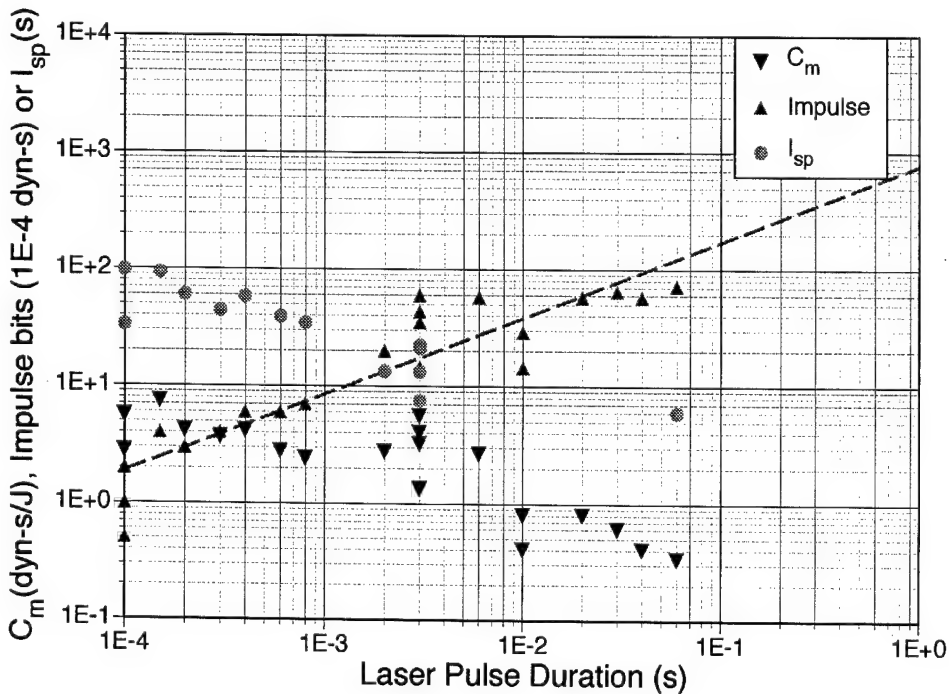
Figure AII.22 [ID13]

Q* data for undeveloped color film, emulsion side up, 5μm spot

This is yet another classic case of rapidly degrading coupling with increasing pulse duration because of a thin absorbing coating (5-10μm) overlying a transparent substrate

Data set ID18: audio tape at focus
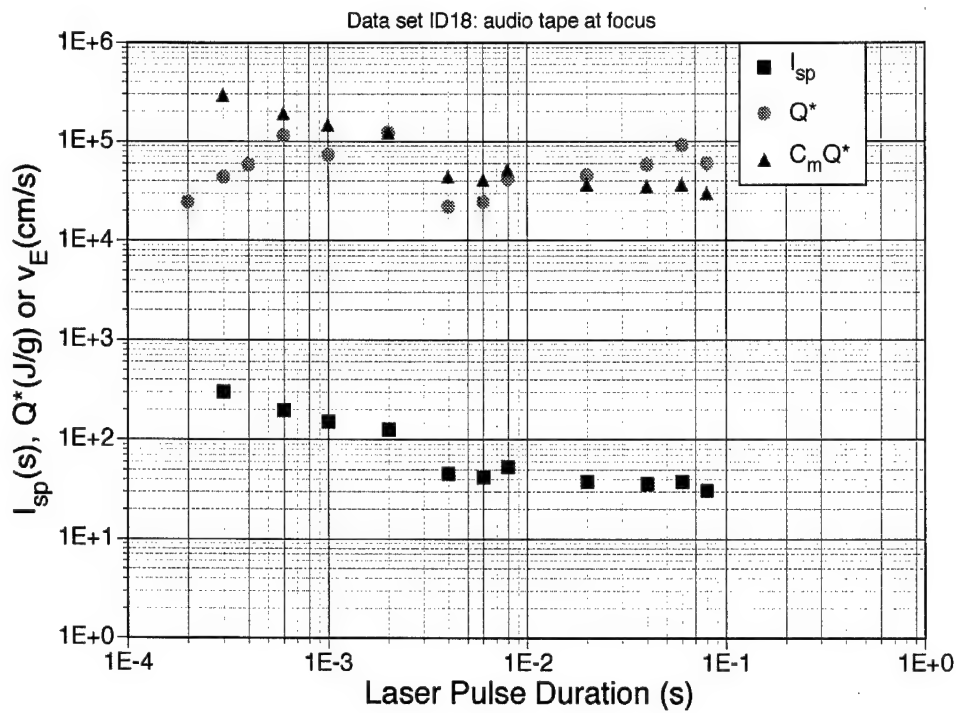
Figure AII.23 [ID18]

Q* data for magnetic tape, emulsion side up, 5μm spot

ID18, audio tape, $d_s = 5.2 \, \mu m$
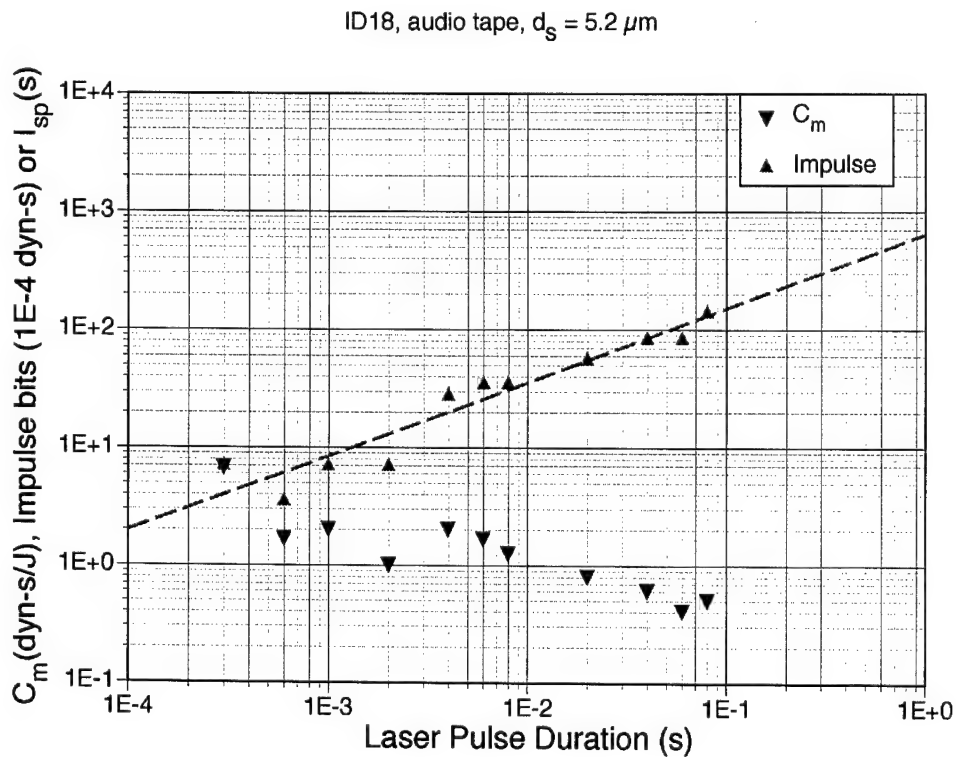
Figure AII.24 [ID18]

C_m data for magnetic tape, emulsion side up, 5μm spot

Same basic behavior as for Figure AII.21 material.

Data set ID19&20: audio tape at 200μm spot size
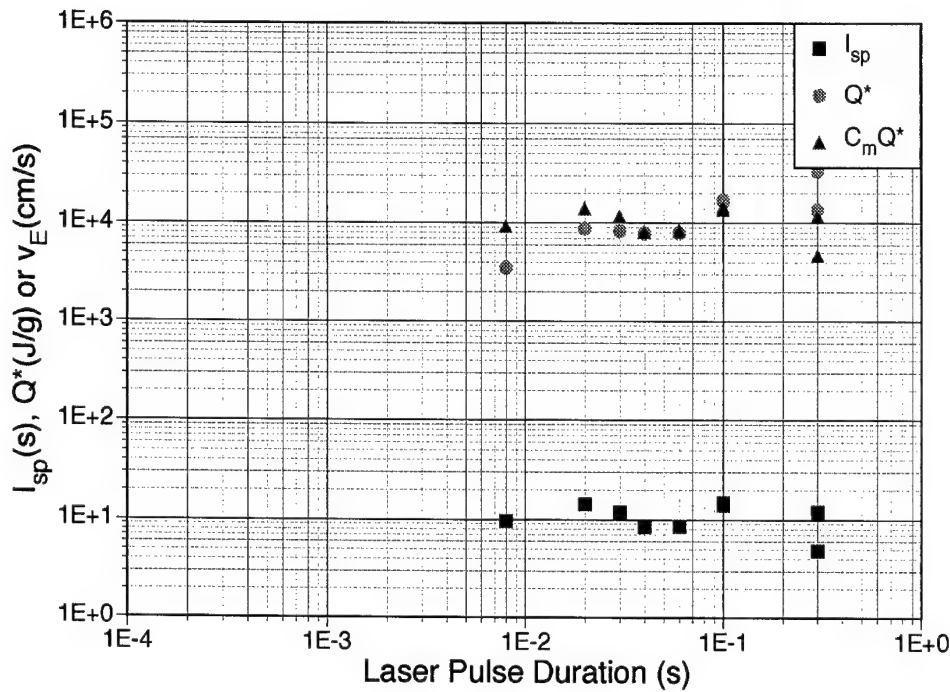
**Figure AII.25
[ID19&20]**

**Q* data for magnetic
tape, emulsion side up,
200μm spot**

I_{sp} is very poor for all pulse
durations tested.

ID19&20, audio tape, d_S = 200 μm
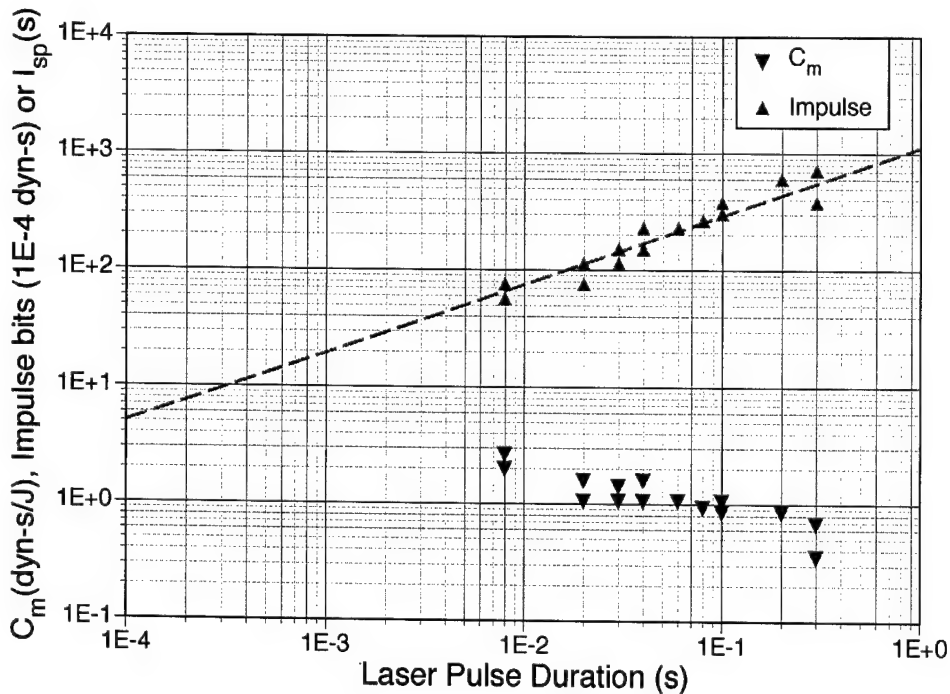
**Figure AII.26
[ID19&20]**

**C_m data for magnetic
tape, emulsion side up,
200μm spot**

C_m is very poor for all pulse
durations tested.

ID40: 300μm Viton oring, d$_s$ = 5.2μm
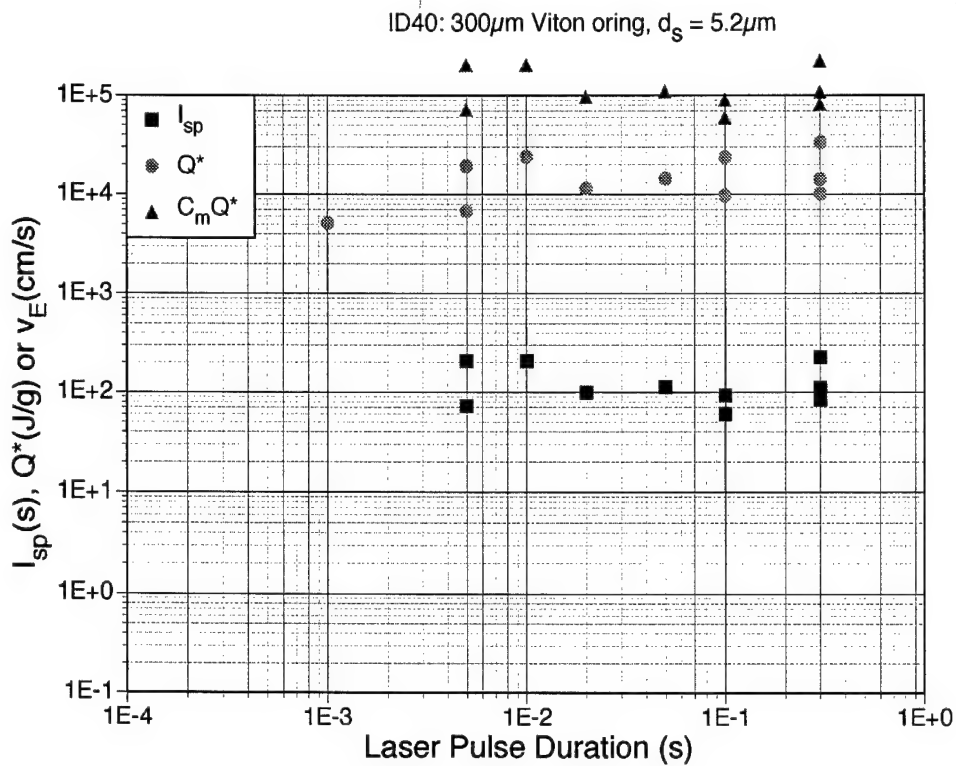
Figure AII.27 [ID40]

Q* data for 900μm Viton slab, 5μm spot

ID40: 300μm Viton oring, d$_s$ = 5.2μm
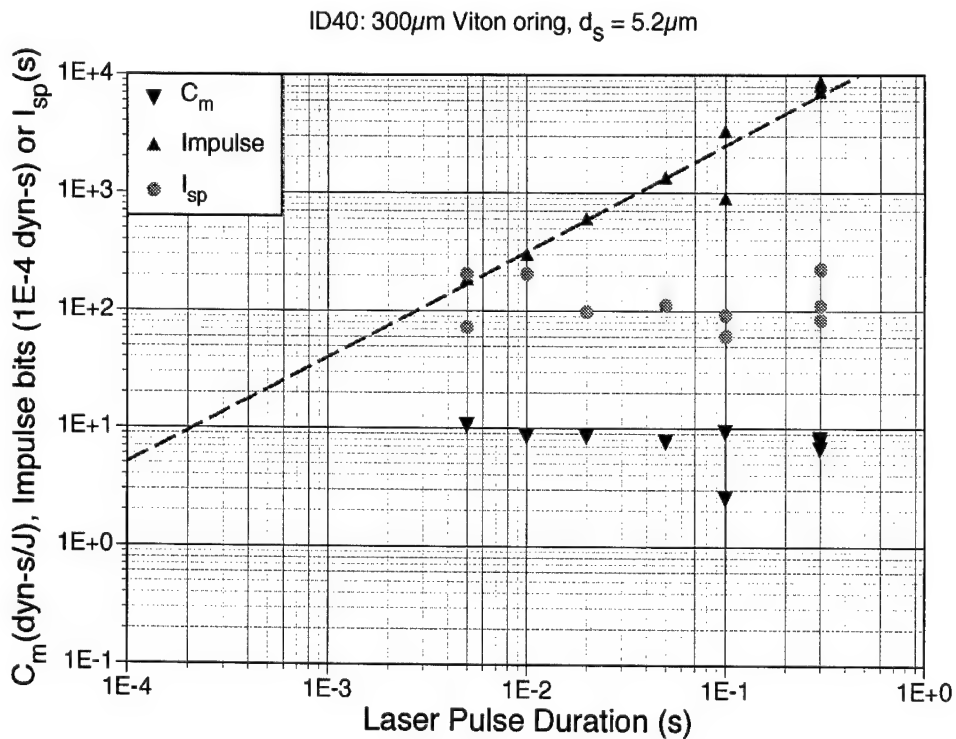
Figure AII.28 [ID40]

C$_m$ data 900μm Viton slab, 5μm spot

Coupling is reasonably good, but I$_{sp}$ is disappointing.

Data Set ID10: Se-black Al foil 5.2μm spot
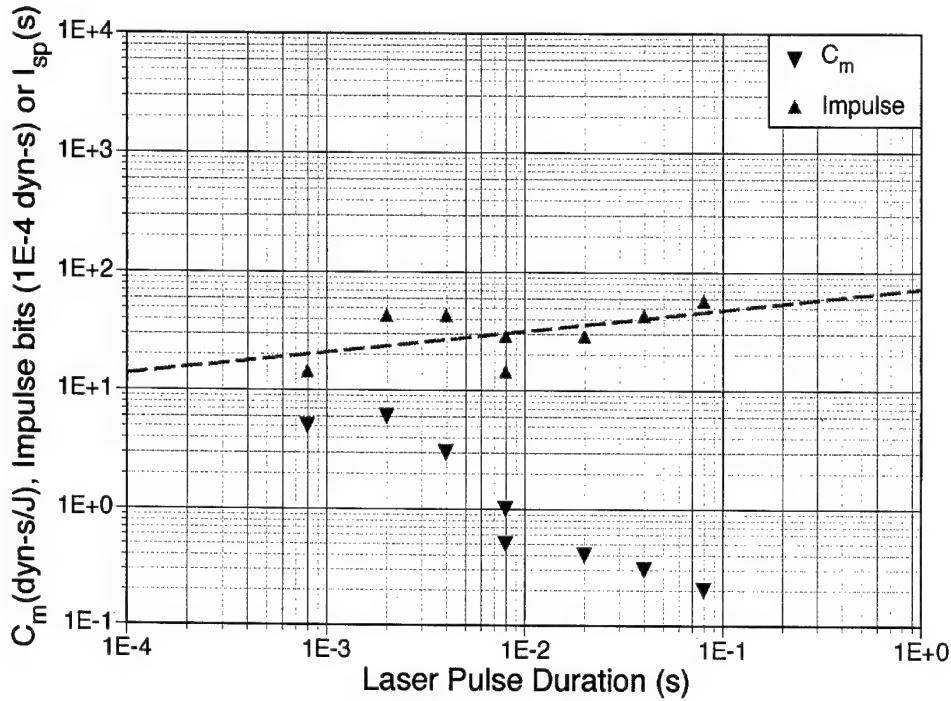
Figure AII.29 [ID10]

Bare 2024 aluminum coated with est. 1μm "selenium black" process coating.

A classic case of rapidly degrading coupling with increasing pulse duration because of a thin absorbing coating overlying a highly reflective substrate.

ID11, black sharpie on saran, $d_S = 5.2 \mu m$
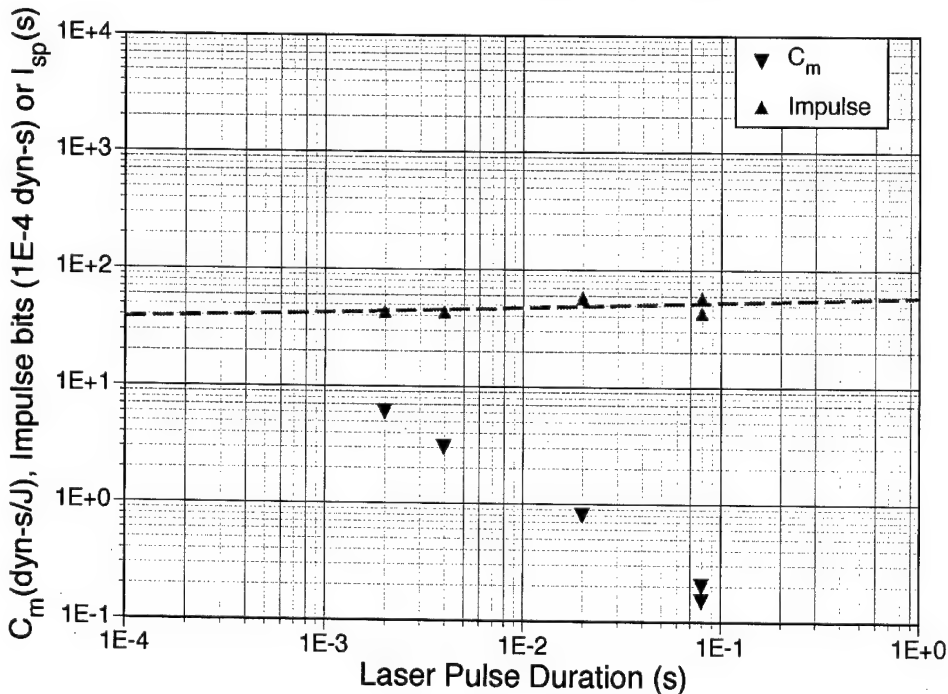
Figure AII.30 [ID11]

Vinyl copolymer ("Saran" wrap) coated with black marking ink, est. 2μm.

One final case of rapidly degrading coupling with increasing pulse duration because of a thin absorbing coating overlying a highly transparent substrate

Outgassing

We operated at typical chamber pressures of 5E-4 torr. All targets reported survived substantial vacuum exposure without any noticeable degradation of mechanical properties or performance. The ablation process did not increase chamber pressure measurably.

Annex III: Laser Momentum Coupling

Table AI.1: Glossary

Symbol	Definition	Value or Equivalence
α	Intensity absorption coefficient for light at the laser frequency in the absorption zone	cm^{-1}
α_{IB}	Inverse bremsstrahlung absorption coefficient	cm^{-1}
C_m	coupling coefficient	dyn-s/J
C_p	Specific heat at constant pressure	$Jg^{-1}K^{-1}$
c_s	Sound speed in the plume near the laser absorption zone	cm/s
C_v	Specific heat at constant volume	$Jg^{-1}K^{-1}$
d_s	Laser $1/e^2$ beam diameter at the surface	cm
E	Substitute for "10^", for ease of reading exponents	-----
η_{AB}	Ablation energetic efficiency	----
ε	Plasma dielectric function	-----
$\in$	Emissivity	-----
F	Constant	2.5E4
Φ	Per-pulse laser fluence incident on the target surface	J/cm^2
g	Acceleration of gravity	$980\ cm/s^2$
γ	C_p/C_v, 5/3 for an ideal gas and 1.2 for ablation vapor	-----
H	$Am_p[q* + C_v(T-T_1)]$, total energy content	J/atom
I_{sp}	Specific impulse	s
k	Boltzmann constant	1.38E-16 erg/K
κ	$K/(\rho C_v)$, thermal diffusivity	cm^2/s
I	Laser intensity	W/cm^2
K	Thermal conductivity	$Jcm^{-1}K^{-1}$
λ	Laser wavelength	cm
m	Constant	0.45
M_A	Average atomic mass number in ablation vapor	amu
$\tilde{n}$	Plasma refractive index	-----
n	Real part of $\tilde{n}$	-----
n_o	Neutral density	cm^{-3}
n_j	Density of species j (electrons, ions, etc.)	cm^{-3}
ν_r	Plasma recombination rate	$cm^{-3}s^{-1}$
p	Impulse	dyne-s
$Q*$	Observed laser energy invested per gram of target ablated	J/g

q^*	$q_f + q_v + C_v T_v$, theoretical energy per gram necessary to reach the threshold of ablation, zero ablation depth limit of Q^* with perfect absorption	J/g
q_f	Heat of fusion	J/g
q_v	Heat of boiling or phase explosion	J/g
q_b	$q_f + q_b$	J/g
θ_d	Vapor beam angle (FWHM) leaving the Knudsen layer	deg
σ_{SB}	Stefan-Boltzmann constant	$5.67E\text{-}12\ Wcm^{-2}K^{-4}$
τ	Laser pulsewidth, FWHM	s
T_e	Electron temperature near surface	K
T	Surface temperature or vapor temperature near surface	K
T_1	Boiling temperature at atmospheric pressure	K
W_L	Per-pulse laser energy	J
W_i	First ionization state energy for target atoms	J
x	Distance into surface or coating thickness	cm
x_I	Thickness of the laser absorption layer	cm
x_T	Thickness of the 1D-2D transition zone	cm
x_{th}	$\sqrt{(\kappa\tau)}$, thermal diffusion depth during laser pulse	cm
v_{AB}	Ablation jet velocity	cm/s
Z	Plasma ionization state	-----
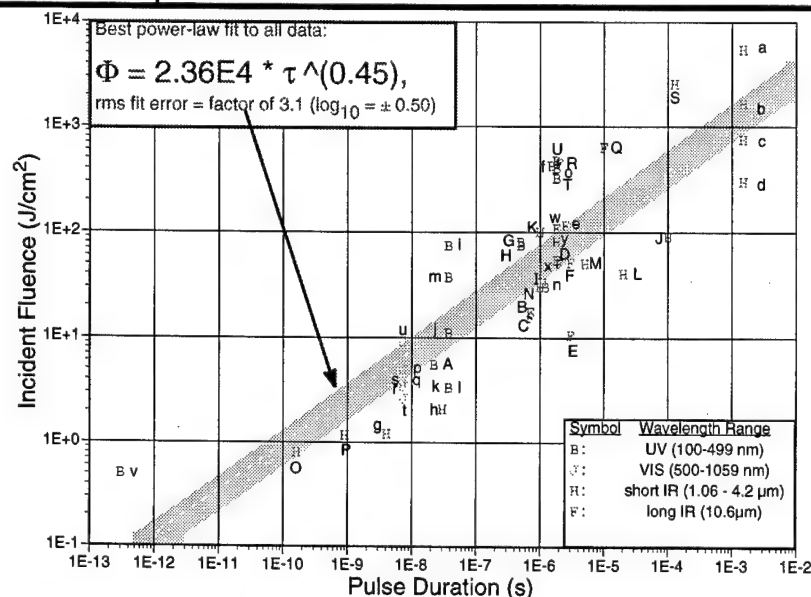
Figure AIII.1. Results of 46 Reported Experiments from the UV to the IR Show the Same Trend for the Fluence Required to Achieve Maximum Coupling. [Phipps 1996].

The momentum coupling coefficient C_m is defined as the ratio of target momentum $m\Delta v$ produced by photoablation to incident laser pulse energy W, by convention expressed in mixed units:

$$C_m = \frac{p}{W_L} \quad \text{dyne-s/J. [AIII.1]}$$

As incident pulsed laser fluence increases past threshold, C_m for a wide variety of materials rises rapidly to a peak value of 2–8 dyne-s/J, declining slowly for higher fluence as ejecta velocity increases. We surveyed the results of 46 experiments in which the fluence Φ_{opt} for optimum coupling was measured, and determined that

42

for a wide variety of possible debris surfaces, wavelengths ranging from 0.25 to 10.6 μm, and pulsewidths 100ps<τ<1ms, Φ_{opt} can be fit by:

$$\Phi_{opt} = F\,\tau^m \qquad \text{J/cm}^2 \qquad\qquad \text{[AIII.2]}$$

Experimentally, m ≈ 0.45, whereas thermal transient theory [Carslaw & Jaeger 1959] would give m = 0.5.

Model above plasma threshold

The basis of this portion of our model is standard plasma physics.

Defining $\qquad\qquad \tilde{n} = n + i\chi$ $\qquad\qquad\qquad$ [AIII.3]

for the plasma complex refractive index and

$$\varepsilon = \tilde{n}^2 = (n^2 - \chi^2) + i\,2\,n\,\chi \qquad\qquad \text{[AIII.4]}$$

as the plasma complex dielectric function, the real (refractive) and imaginary (absorptive) parts of the dielectric constant, ε, of a nonmagnetized plasma are given by

$$\text{Re}(\varepsilon) = n^2 - \frac{\omega_p^2}{\omega^2\,(1 + v^2/\omega^2)} \qquad\qquad \text{[AIII.5]}$$

and $\qquad\qquad \text{Im}(\varepsilon) = \frac{v}{\omega}\left[\frac{\omega_p^2}{\omega^2\,(1 + v^2/\omega^2)}\right] \qquad\qquad$ [AIII.6]

so that the optical absorption coefficient is:

$$\alpha = \frac{2\omega}{c}\chi = \frac{v}{nc}\left[\frac{\omega_p^2}{\omega^2\,(1 + v^2/\omega^2)}\right] \qquad , \qquad\qquad \text{[AIII.7]}$$

and $\qquad\qquad \varepsilon \approx \tilde{n}^2 \approx [1 - n_e/n_{ec}].$ $\qquad\qquad\qquad$ [AIII.8]

When collisions are small compared to the optical frequency (v/ω<<1) as is usually true for laser-produced plasma, the refractive index goes to zero and complete reflection occurs at the "critical electron density"

$$n_{ec} = m_e n^2 \omega^2/4\pi e^2 = 1.115\,\text{E}21/\lambda_{\mu m}^2 \qquad\qquad \text{cm}^{-3}. \qquad\qquad \text{[AIII.9]}$$

Applying these results to opaque materials in vacuum irradiated by pulsed lasers at or <u>above plasma threshold</u> intensity (Phipps et al. 1988), gives pressure, temperature and coupling coefficient C_m to good accuracy for a broad range of irradiation conditions [Phipps et al 1988].

The principal results of that work which we use here are:

$$p_{AB} = 5.83 \; \frac{\Psi^{9/16}}{A^{1/8}} \frac{I^{3/4}}{(\lambda\sqrt{\tau})^{1/4}} \qquad \text{dyn/cm}^2 \qquad \text{[AIII.10]}$$

and
$$T_e = 2.98 \times 10^4 \; \frac{A^{1/8} \; Z^{3/4}}{(Z+1)^{5/8}} \; (I\lambda\sqrt{\tau})^{1/2} \quad K \qquad \text{[AIII.11]}$$

for the plasma electron temperature where $2\Psi = A/[(Z^2(Z+1)]^{1/3}$, and $\Psi \leq 1$ for nearly every case with the longer pulses in this project. For coupling coefficient we have:

$$C_m = 3.95 \; M_A^{0.44}/[Z^{0.38}(Z+1)^{0.19}(I\lambda\sqrt{\tau})^{0.25}]. \qquad \text{[AIII.12]}$$

Model below plasma threshold

Below plasma threshold, in the vapor-dominated regime, C_m can be calculated via a Clausius-Clapeyron relation:

$$p(atm) = \frac{p}{p_1} = \exp\left[\frac{H_1}{kT_1} - \frac{H}{kT}\right] \qquad \text{[AIII.13]}$$

Eqn. [AIII.6] may be rewritten in a simpler form with temperature T as a free variable:

$$\ln p(atm) = \frac{M_A}{k} \left[\left(\frac{q^*}{T_1} - C_v\right) + \left(\frac{C_v T_1 - q^*}{T}\right)\right]. \qquad \text{[AIII.14]}$$

The following relationship connects laser intensity I to the material variables:

$$I = \rho v_{AB}[q^* + C_p(T_{vapor} - T_1) + v_{AB}^2/2] + (x_{skin} + x_{th})\rho_s C_v(T_1 - T_0)/\tau + \in \sigma_{SB}T^4. \qquad \text{[AIII.15]}$$

Taking the five terms in sequence, these energy sinks are 1) providing the vaporization energy q^* to an element of vapor, 2) further heating the vapor after it leaves the surface, 3) accelerating the vapor, 4) heating a final element of surface of thickness $(x_{skin} + x_{th})$ to temperature T_1 from room temperature T_0 which is left behind without vaporization at the end of the laser pulse, and 5) black body emission with emissivity $\in$ from the half-plane facing the laser.

If we now let $p_{vap} = p$, $T_{vap} = T$, and vary T, the result can then be presented as a plot of p vs. I for a target material with a chosen laser pulsewidth, from which the vapor phase value of C_m can be obtained [Figure AIII.2].

The crossover between these regimes in our model is smooth, showing that both predictions are good in their respective limits.

General considerations

Two other quantities which are often used to describe laser ablation and laser propulsion are Q^*, the incident laser energy (J/g) required to ablate unit mass of target material, and I_{sp} (s), familiar from rocketry as specific impulse. It is important to realize that the two elements of the pairs (C_m, Q^*) and (C_m, I_{sp}) are not independent, but increasing one decreases the other.

$$C_m Q^* = v_E = g I_{sp}, \qquad \text{[AIII.16]}$$

and
$$C_m I_{sp} = C_m^2 Q^*/g = 20,394 \; \eta_{AB} \quad , \qquad \text{[AIII.17]}$$

where v_E is the exhaust velocity of the ablation jet. Eqn. [AIII.17] permits I_{sp} for laser ablation jets

Ink 0.1cm,
R=0.1
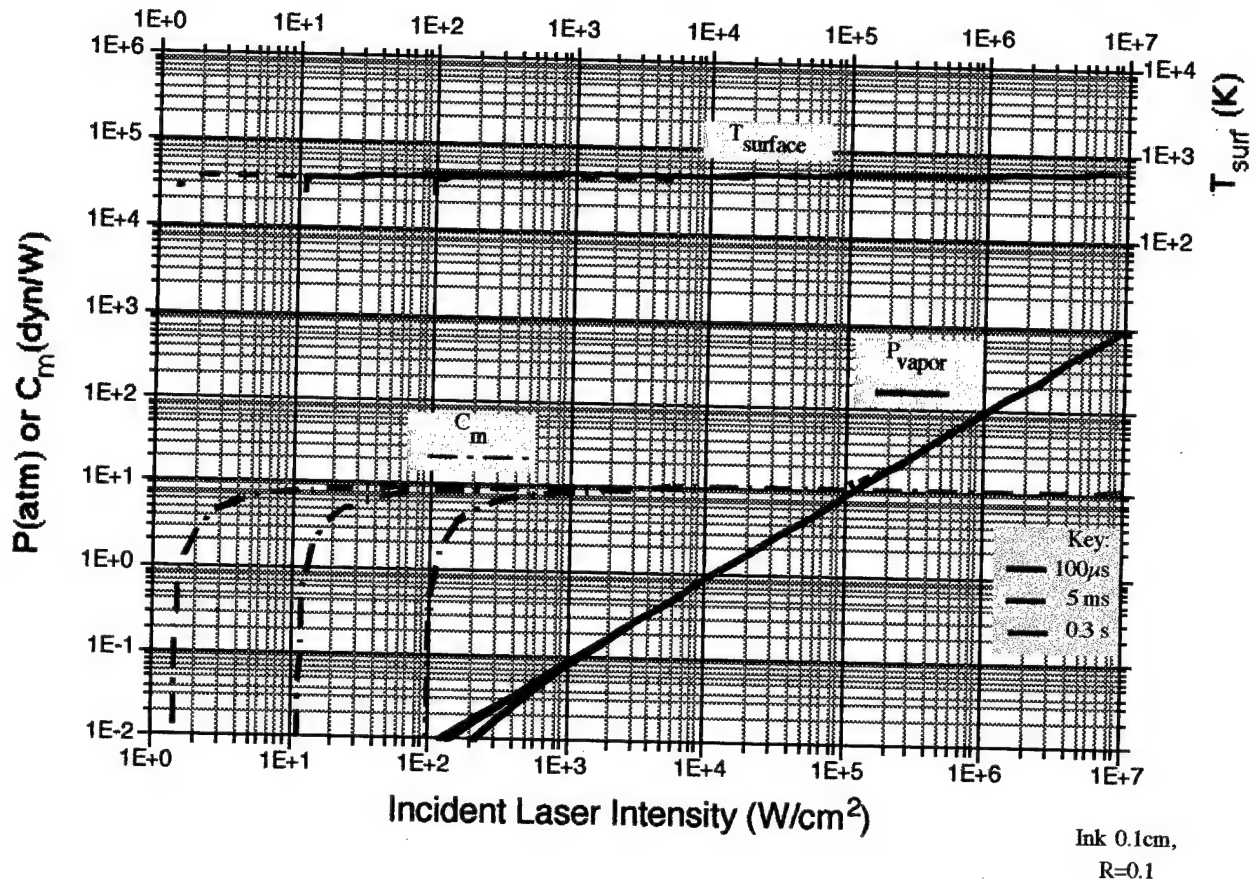
Figure AIII.2: Surface pressure, temperature and coupling coefficient C_m predicted by our model, vs. incident laser intensity for black ink and pulse duration = $100\mu s$, 5ms & 300ms.

to achieve values much larger than those available in chemical reactions. Experimental results as large as 7,000 seconds have been achieved in other reported work [Phipps et al. 1994].

Figure AIII.2 shows good agreement with results we measured from the type of targets we have used in this STTR project, in which the laser absorbing surface is black ink and the substrate has low thermal diffusivity (paper, mylar, etc.). Note that the surface temperature in the Figure AIII.2 simulation is just that - the temperature of the solid/vapor interface at the ablating surface.

Above plasma threshold in the vapor, surface temperature would not be much different, but laser heating of the vapor continues until temperatures of 10,000 - 20,000K are achieved.

This model (described above) shows no transition to plasma regime at the largest intensities we achieved with our 1-W laser. Other considerations, treated in Annex V, enter into determining where this transition occurs.

Practically speaking, it is easy to obtain C_m = 10 dyne-s/J [1E-4 n-s/J] from the ink-like target materials we have studied for a 1-dimensional interaction, and possible to obtain C_m = 20-25, given spot size much smaller than the target, so that the laser-induced pressure wave expands across the target until it dissipates. We regard agreement with our simulations as very good.

References

Campbell, J. W., NASA Marshall Spaceflight Center Technical Memorandum 108522 (1996)

Carslaw, H.S. and Jaeger, J.C. 1959 Conductin of Heat in Solids Clarendon, Oxford

Phipps, C.R. and Michaelis, M.M. 1994, "LISP," *Laser and Particle Beams,* **1 2** (1), 23-54

Phipps, C. R., AIP Conf. Proceedings 318 pp. 466-8 (1993)

Phipps, C.R., Harrison, R.F., Shimada, T., York, G.W., Turner, T.P., Corlis, X.F., Steele, H.S., Haynes L.C. and King, T.R. 1990, "Enhanced Vacuum Laser-impulse Coupling by Volume Absorption at Infrared Wavelengths", *Laser and Particle Beams,* **8**, 281

Phipps, C.R., Turner, T.P., Harrison, R.F., York, G.W., Osborne, W.Z., Anderson, G.K., Corlis, X.F., Haynes, L.C., Steele, H.S., Spicochi, K.C., and King, T.R. 1988, "Impulse Coupling to Targets in Vacuum by KrF, HF and CO2 Lasers" , J. Appl. Phys., **6 4**, 1083
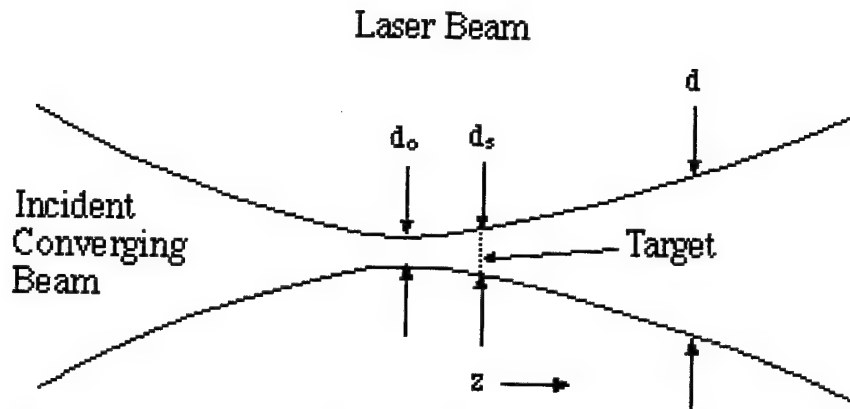
Annex IV: Average Fluence

Laser Beam

Figure AI.1: Illustrating parameters of analysis

With the lightweight pendulum, target acceleration leads to substantial target motion during the longer laser pulses. It was important to be able to correct data when this variation was slight, as well to indicate when it was necessary to use the heavy pendulum to get a meaningful measurement of C_m vs. fluence in a given case.

Further, in about half the shots we deliberately chose $d_{s1} \gg d_o$, say 200μm instead of 5μm, to obtain data for coupling for a range of fluence as well as pulsewidth. In such a case, the variation might be less severe. With so many variables, we needed an analytical method of determining the fluence variation during a pulse.

Taking

$$<\Phi> = \frac{1}{\tau}\int_0^\tau dt\ \Phi(t)$$

$$= \frac{4\,W_L}{\pi\,\tau}\int_0^\tau \frac{dt}{d^2(t)} \qquad \text{[AIV.1]}$$

$$d^2(t) = d_o^2 + \left(\sqrt{d_s^2 - d_o^2} + \frac{z}{f_\#}\right)^2 \quad \text{[AIV.3]}$$

$$d_1 = \sqrt{d_s^2 - d_o^2} \qquad \text{[AIV.4]}$$

$$<\Phi>$$

$$= \frac{4\,W_L\,f_\#^2}{\pi\,\tau}\int_0^\tau \frac{dt}{(f_\#\,d_1 + z)^2 + (f_\#d_o)^2}$$

$$= C\int_0^\tau \frac{dt}{(\alpha + \beta t^2)^2 + \gamma^2} \qquad \text{[AIV.5]}$$

Table AI.1: Glossary

Sym-bol	Definition	Value or equivalence
C_m	coupling coefficient	dyn-s/J
d_{s1}	Starting spot size	cm
d_{s2}	Ending spot size	cm
d_o	Minimum spot size	cm
E	Fiber Young's modulus	7.08E11 dyn/cm^2
$f_\#$	Illumination f-number	(f/d$_s$) ---
f	Illumination focal length	cm
Φ	Laser fluence on target	J/cm^2
m	Effective mass at radius R	gm
n/m	not measured	
p	Impulse	dyn-s
θ	Rotation angle	rad
θ_o	Rotation amplitude	rad
R	Impulse moment arm	2 cm
τ	Pulse duration	s
W_L	Incident laser energy	J
ω_o	Resonant frequency	$2\pi f_o$ rad/s

where

$$C = \frac{4\,W_L\,f_\#^2}{\pi\,\tau} \qquad \text{and} \qquad \gamma = f_\# d_o \qquad \text{[AIV.6]}$$

$$\alpha = f_{\#} d_1 \qquad \text{and} \qquad \beta = \frac{\omega_o \theta_o R}{2\tau} \qquad \text{[AIV.7]}$$

and we have taken

$$z = \frac{\ddot{z} t^2}{2} \qquad \text{and} \qquad \ddot{z} = \frac{\omega_o \theta_o R}{\tau}. \qquad \text{[AIV.8]}$$

The integral AIV.5 is tabulated [Gradshteyn & Ryzhik 1965] and the result is:

$$<\Phi> = \frac{C}{4\beta^2 q^3 \sin\psi} *$$

$$\left[\sin(\psi/2) \ln\left(\frac{t^2 + 2qt\cos(\psi/2) + q^2}{t^2 - 2qt\cos(\psi/2) + q^2} \right) + 2\cos(\psi/2) \tan^{-1}\left(\frac{t^2 - q^2}{2qt\sin(\psi/2)} \right) \right] \Bigg|_0^\tau \qquad \text{[AIV.9]}$$

with notations $\quad \psi = \cos^{-1}\left[-1 / \sqrt{[1 + (\gamma/\alpha)^2]} \right] \qquad$ and $\qquad q^2 = \frac{\sqrt{\alpha^2 + \gamma^2}}{\beta} \qquad \text{[AIV.10]}$
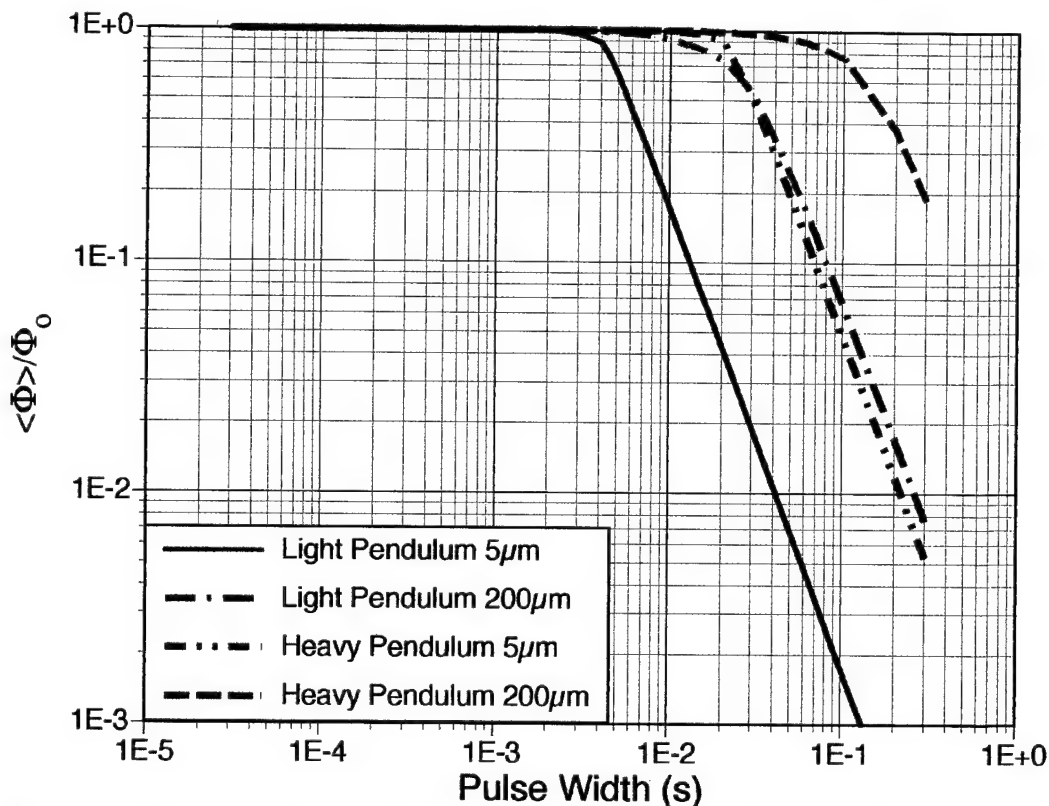
Figure AIV.1: How target motion during laser pulse affects average fluence for the two pendula and two initial spot sizes

Reference

1. Gradshteyn, I. S. and Ryzhik, I. M.(1965), *Table of Integrals, Series and Products*, Academic, New York § 2.161.1b

Target Matrix

Table AIV.1. Maximum Values of Average Fluence

| Test Nos	Target	d_s (μm)	t (μm)	Pend. Lt	Pend. Hvy	Pulse width Min (ms)	Pulse width Max (ms)	Φ_o Max J/cm²	Φ_g Gold Bar J/cm²	Φ_o/Φ_g
4,12	Black printer's ink:paper	5	350	X		0.1	40	1.70E+3	5.54E+3	0.307
30	Black printer's ink:paper	5	350		X	100	300	3.12E3	1.37E+4	0.228
6	Black printer's ink:paper	100	350	X		0.8	60	3.40E+2	6.65E+3	0.051
17	Black printer's ink:paper	200	350	X		0.2	50	4.30E+1	6.13E+3	0.007
21,22	Black printer's ink:paper	200	350		X	10	300	3.64E+2	1.37E+4	0.027
9,16	Xerographic black:paper	5	100	X		0.1	80	4.64E+3	7.57E+3	0.613
24	Xerographic black:paper	200	100		X	5	300	1.50E+2	1.37E+4	0.011
41,46	Thin PVC film	5	175	X		0.1	5	3.55E+3	2.17E+3	1.632
37	Thin PVC film	5	175		X	1	300	8.55E+3	1.37E+4	0.623
38	Thin PVC film	200	175	X	X	2	300	8.90E+1	1.37E+4	0.006
44	Thick PVC film	5	500	X		0.1	20	2.20E+3	4.06E+3	0.542
8	Phenolic resin	5	250	X		0.8	100	5.56E+3	8.37E+3	0.664
29	Phenolic resin	5	250		X	2	300	---	1.37E+4	
31	Phenolic resin	200	250		X	10	300	1.53E+2	1.37E+4	0.011
47,48	Black ink: mylar	5	50	X		0.05	1	3.13E+2	1.05E+3	0.297
23	Black ink: mylar	200	50		X	2	300	2.30E+2	1.37E+4	0.017
25	Black ink: mylar sandwich	200	100		X	---	300	2.30E+2	1.37E+4	0.017

Test Nos	Target	d_s (μm)	t (μm)	Pend.			Pulse width		Φ_o	Φ_g	Φ_o / Φ_g
				Lt	Hvy		Min (ms)	Max (ms)	Max J/cm^2	Gold Bar J/cm^2	
43	Black ink:glass	5	90	X			0.1	20	1.35E+3	4.06E+3	0.333
42	Black ink:glass	100	90	X			0.1	20	4.70E+1	4.06E+3	0.012
32	Black thin polyethylene	5	100		X		5	300	6.50E+4	1.37E+4	4.735
34	Black thick polyethylene	5	850		X		50	300	2.00E+4	1.37E+4	1.457
45	Kapton	5	125	X			0.2	200	6.50E+3	1.14E+4	0.568
13	Photographic film	5	175	X			0.1	60	8.54E+3	6.65E+3	1.283
18	Audio tape	5	50	X			0.1	80	7.90E+3	7.57E+3	1.043
19,20	Audio tape	200	50	X	X		8	300	3.00E+2	1.37E+4	0.022
26	Graphite sheet	5	380		X		100	300	2.00E+4	1.37E+4	1.457
40	Viton	5	300		X		1	300	4.80E+4	1.37E+4	3.496
10	Se black:Al	5	100	X			0.8	80	4.05E+4	7.57E+3	5.017
11	Black ink:vinyl copolymer	5	25	X			0.8	80	4.05E+4	7.57E+3	5.348
33	Cellulose nitrate	5	70		X		2	300	9.24E+4	1.37E+4	6.733
39	Black anodize:Al	5	500		X		2	300	9.24E+4	1.37E+4	6.733
36	Fiberglas	5	1500		X		2	300	9.24E+4	1.37E+4	6.733

The Table, adapted from Table AII.1, compares the maximum average fluence values achieved in all data sets with the "gold bar" predictions of Figures 10 of the report and Figure AIII.1. We were not able to exceed the "gold bar" values by very much with the 1-watt laser. These data are also plotted in the Figure following.
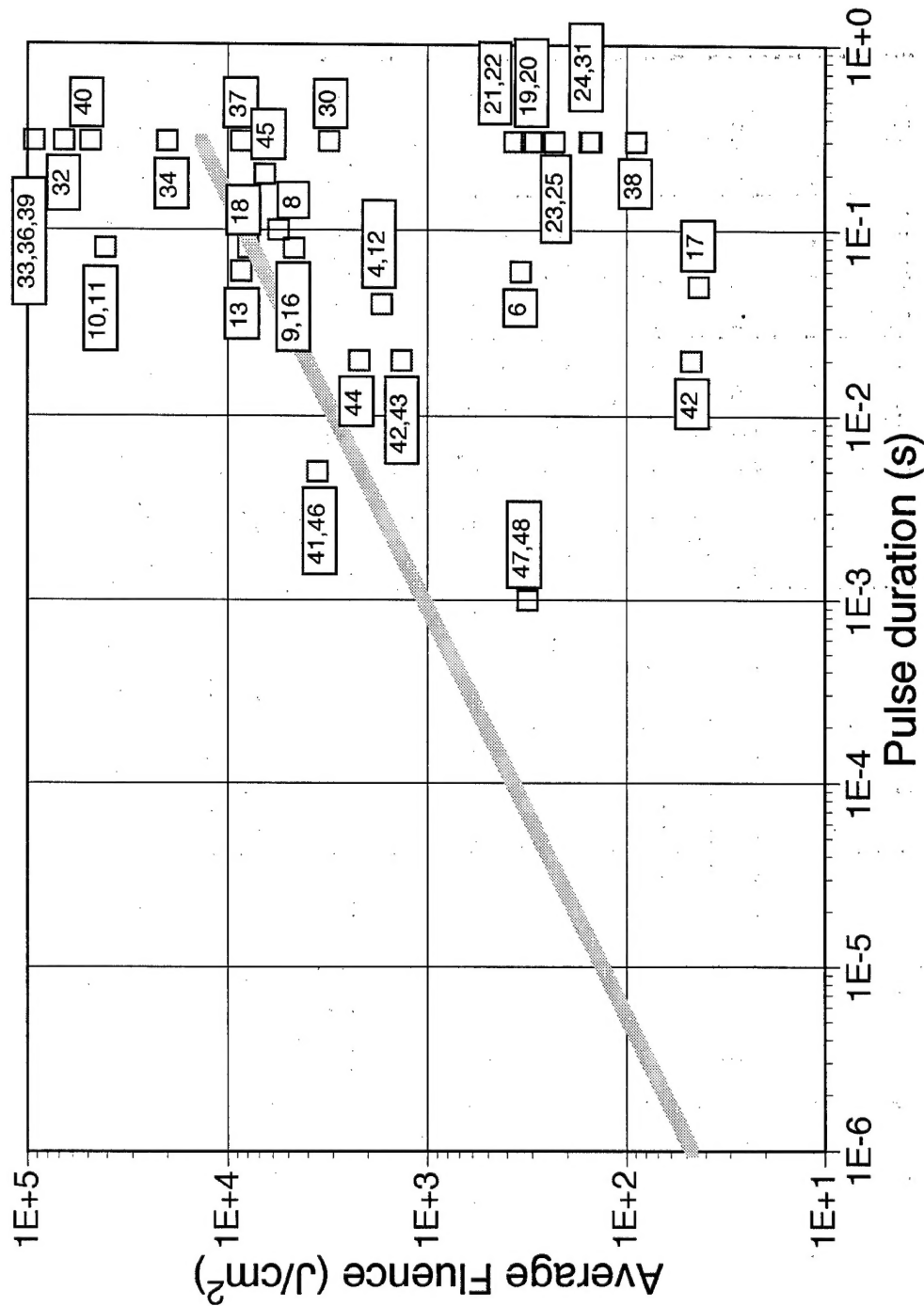
Figure AIV.2. Maximum averge fluence for all data sets [boxes] values achieved vs. "Gold Bar" values

Those targets which we subjected to the highest average fluence were, with one exception, the most refractory, generating zero or very small impulse: polyethylene, fiberglas, bare aluminum, aluminum with a thin selenium-black process coating and vinyl copolymer (saran wrap). The exception is viton, data set 40, which generated reasonably good coupling.
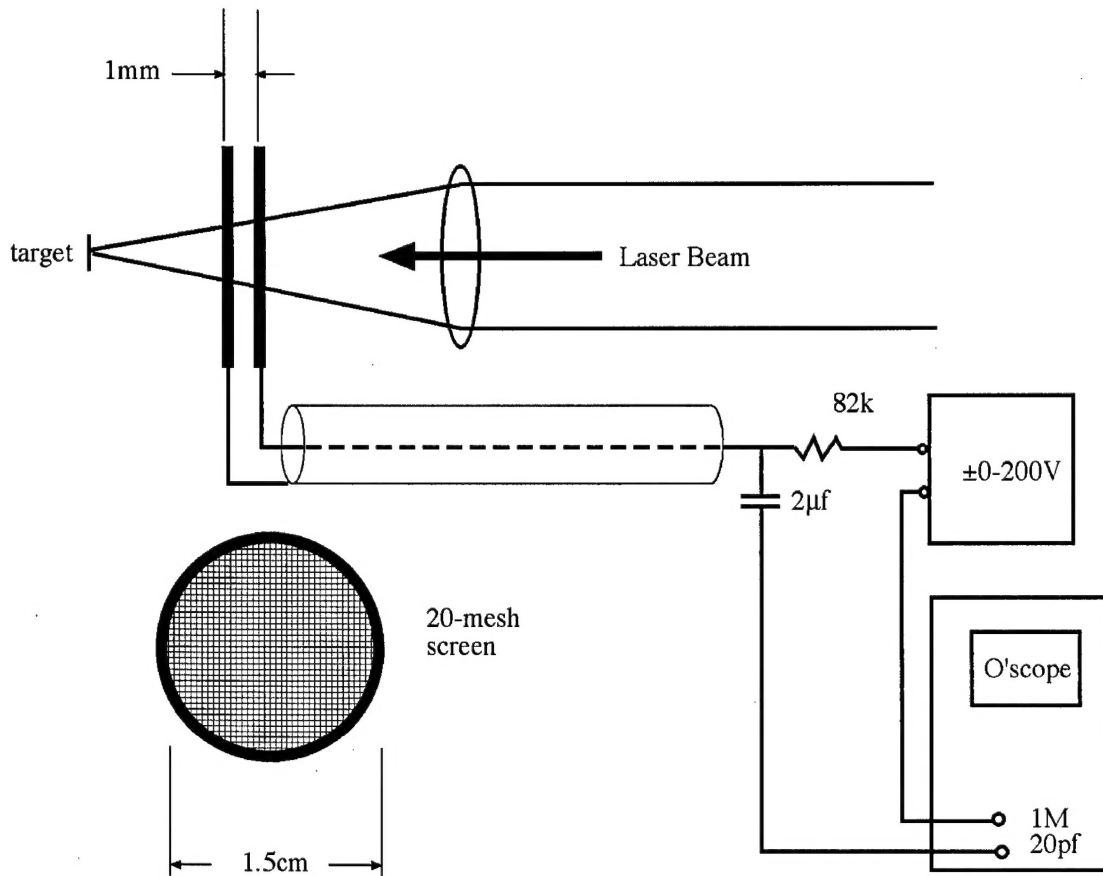
Annex V: Plasma Parameters [objectives f, g]

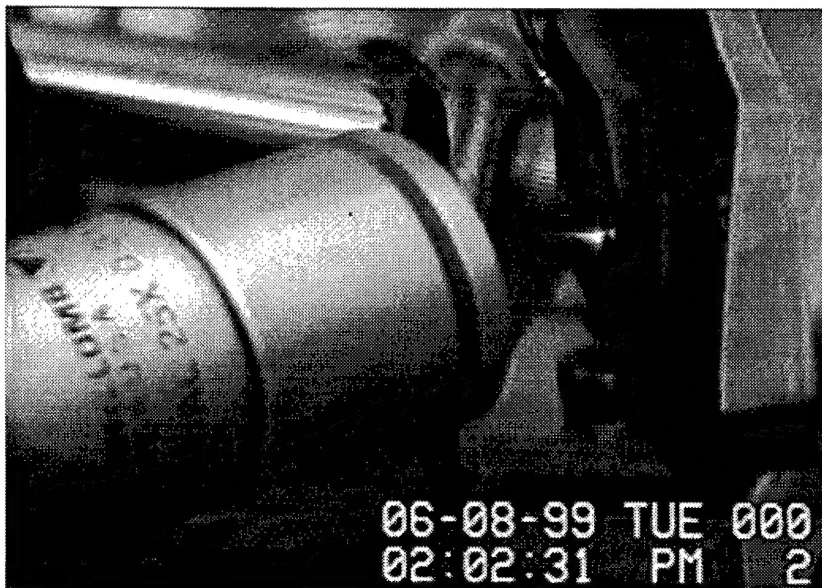**Figure V.1. Plasma Detector**

Figure V.2. [obective. g] The LPT jet is seen (at the focus of the 25X microscope objective). The polar distribution of the plume occupyies less than 0.005 sterrad.

Plasma detector

We built an efficient plasma detector [Figure V.1] with a coarse screen that permitted it to be inserted directly in the beam without degrading the focus significantly. The result was negative during the time available for study of plasma formation.

Analysis: Our negative result is not due to the situation $\lambda_{en} \gg d_s$. From the point of view of laser-induced ionization avalanche, the region near the target still looks 1-dimensional, small though it is. Instead, it is due to the much greater importance of lateral and axial thermal conduction for $5\mu m$ spots, together with relatively long

52

Table V.1. Plasma Test parameters	
Solid angle subtended	1 sterrad
Pulse duration τ	20 ms
Signal V	<10mV
Signal Current I	<120nA = 7.5E11 e^-/s
Target	PVC film
Ablation volume (by inspection)	67 μcm^3/shot
No. of atoms ablated	1.1E16/shot
Ablation rate R	5.5E17/s
Predicted plume temperature	0.1 eV
Predicted plume velocity v_{thi}	9.0E4 cm/s
Plume cone angle (full)	20 degrees
Plume density near detector n_{od}	2.8E13 cm^{-3}
Ionization fraction $\eta_i = I/R$	<1.4E-6
Plasma density near detector n_{ed}	< 3.8E7 cm^{-3}
Plume density at target n_{oT}	2.8E19 cm^{-3}
Neutral cross-section σ	5E-15 cm^2
Electron-neutral mean free path at target $\lambda_{en} = 1/(n_{oT}\sigma)$	0.07μm
Electron Debye screening distance at detector $\lambda_{Ded} = 745 \, [T_{e(eV)}/n_{ed}]^{1/2}$	>380μm
Electron plasma frequency near detector $v_{ped} = 8978(n_{ed})^{1/2}$	<55MHz

pulses. Table V.2 above quantifies this point.

In the absence of plasma, further effort on the plasma topic was not warranted.

2. Optical diagnostics

Optical diagnostics consisted of a magnified view of the plume recorded with a high performance video camera.

Table V.2. Comparing thermal diffusion distance to d_s=5µm for two pulse durations and several materials

Material	K	C	ρ	κ (cm²/s)	x_{1th}(100µs)	x_{1th}/d_s	x_{2th}(300ms)	x_{2th}/d_s
PMMA			1.15	0.000124	1.11E-4	*2.22E-1*	6.10E-3	1.22E+1
Vinylidene chloride (saran)	9.2E-4	1.339	1.744	0.000394	1.98E-4	*3.96E-1*	1.09E-2	2.17E+1
Kevlar Epoxy			1.184	0.000806	2.84E-4	*5.68E-1*	1.55E-2	3.11E+1
Celluloid			1.321	0.000950	3.08E-4	*6.16E-1*	1.69E-2	3.38E+1
PVC	1.7E-3	1.213	1.439	0.000974	3.12E-4	*6.24E-1*	1.71E-2	3.42E+1
Polystyrene	1.6E-3	1.088	1.080	0.001360	3.69E-4	*7.38E-1*	2.02E-2	4.04E+1
Cellulose acetate	3.3E-3	1.757	1.329	0.001410	3.75E-4	*7.50E-1*	2.06E-2	4.11E+1
Acrylic	2.2E-3	1.213	1.190	0.001520	3.90E-4	*7.80E-1*	2.14E-2	4.27E+1
Mica	6.9E-3	0.863	3.0	0.002670	5.17E-4	1.03E+0	2.83E-2	5.66E+1
Silica			2.2	0.008400	9.17E-4	1.83E+0	5.02E-2	1.00E+2
Porcelain	0.16	1.088	2.4	0.061300	2.48E-3	4.96E+0	1.36E-1	2.71E+2
Stainless Steel	0.23	0.460	6.809	0.073400	2.71E-3	5.42E+0	1.48E-1	2.97E+2
Carbon Phenolic			1.432	0.160000	4.00E-3	8.00E+0	2.19E-1	4.38E+2
Lead	0.34	0.134	11.342	0.224000	4.73E-3	9.46E+0	2.59E-1	5.18E+2
tungsten carbide	0.88	0.234	15.223	0.247000	4.97E-3	9.94E+0	2.72E-1	5.44E+2
Silicon	0.84	0.668	2.33	0.540000	7.35E-3	1.47E+1	4.02E-1	8.05E+2
aluminum alloys 2000	2.0	0.962	2.70	0.770000	8.77E-3	1.75E+1	4.81E-1	9.61E+2
magnesium	1.40	1.025	1.74	0.785000	8.86E-3	1.77E+1	4.85E-1	9.71E+2
Copper	3.91	0.385	8.94	1.140000	1.07E-2	2.14E+1	5.85E-1	1.17E+3
graphite	1.64	0.682	1.522	1.580000	1.26E-2	2.52E+1	6.88E-1	1.38E+3

Conclusion:

Good correlation is found between the condition $x_{th}/d_s < 1$ for the shortest pulses we used (italics) and ability to obtain photoablation on the types of target materials we studied.